

Voids in Redshift Space

Masatoshi Shoji^a and Jounghun Lee^b

^aTexas Cosmology Center and Department of Astronomy, The University of Texas at Austin, Austin, TX 78712, USA

^bDepartment of Physics and Astronomy, FPRD, Seoul National University, Seoul 151-747, Korea

E-mail: mshoji@astro.as.utexas.edu, jounghun@astro.snu.ac.kr

Abstract. We study the ellipticity probability distribution function (PDF) of voids in redshift space with galaxies as tracers of the shapes of voids. We find that the redshift space distortion on the shape of voids statistically increases the ellipticities of voids, and leaves a prominent feature on the ellipticity PDF as a substantial reduction in the probability of having voids with small ellipticity. The location of this characteristic cutoff of the ellipticity PDF is an explicit function of the logarithmic growth rate, $f(z) \equiv \frac{d \ln D_+(z)}{d \ln a(z)}$, and it can be used as a probe of cosmology once the radial density profile of voids is better understood. However, the biggest limiting factor for the use of ellipticity PDF as a probe of cosmology lies in the Poisson noise from a small number of galaxies to define the shape of a given void. This Poisson noise creates a significant contamination of the resulting ellipticity PDF so that the shape of the original PDF is almost washed-out. Nevertheless, there is a way to overcome the Poisson noise via the Alcock Paczynski test on the shape of stacked voids. In redshift space, since the void is elongated toward the line of sight, the stacked void has non-zero ellipticity, which can be a tell-tale of the logarithmic growth rate. Although some useful information of void ellipticity will be lost by stacking, in this way, we can see the effect of redshift space distortion as a source of anisotropy in the stacked void ellipticity. We think that the stacking analysis of the voids in redshift space is potentially a powerful tool to probe the cosmology.

Keywords: dark energy experiments, galaxy surveys, cosmic web, redshift surveys

Contents

1	Introduction	1
2	Void in the real space	3
2.1	Real-Space Ellipticity PDF	4
3	Linear Galaxy Bias in the Real-Space Void ellipticity PDF	8
4	Void in the redshift space	10
4.1	Spherical Void	12
4.2	Spheroidal Void	13
4.3	Redshift-Space Ellipticity Distribution Function	15
4.4	Void With General Radial Density Profile	17
5	Effect of Void Finding and Poisson Noise on the Void Ellipticity PDF	17
5.1	Void With a Well-defined Boundary: $\langle p_i \rangle \rightarrow P_i$	20
5.2	Void With an Undefined Boundary: $\langle p_i \rangle \neq P_i$	21
6	Voids from N-body Simulation	24
6.1	Comments on the Void-Finder Dependence	26
7	Discussion and Conclusion	28
A	Calculation of $\kappa(\mathbf{x})$	29
A.1	Spherical Void	30
A.2	Spheroidal Void with azimuthal symmetry	32
B	List of Y_l^m, j_l and Wigner-3J symbols used in appendix A	38

1 Introduction

The abundance of on-going and future galaxy surveys is pointing to the deeper understanding of the nature of accelerated expansion of the universe, as discovered via observations of luminosity distances to Type Ia supernovae [30, 32]. The main observables of galaxy surveys are characteristic length scales encoded in the matter power spectrum, $P(k)$, such as the comoving Hubble horizon, $H(z)$, and the angular diameter distance, $D_A(z)$ [37].

Not only can we measure geometric distances, $D_A(z)$ and $H(z)$, from a galaxy survey, but we also measure the growth rate of the matter density fluctuation, $f(z) \equiv \frac{d \ln D_+(z)}{d \ln a(z)}$, via redshift space distortions [10].

The matter density fluctuation grows via gravitational instability competing against the expansion of the universe. One can obtain the growth rate by solving the following differential equation [18, 24, 40],

$$\begin{aligned} \frac{d^2 g}{d \ln a^2} + \left[\frac{5}{2} + \frac{1}{2} (\Omega_k(a) - 3w(a)\Omega_{DE}(a)) \right] \frac{dg}{d \ln a} \\ + \left[2\Omega_k(a) + \frac{3}{2} (1 - w(a)) \Omega_{DE}(a) \right] g(a) = 0, \end{aligned} \quad (1.1)$$

where

$$g(a) \equiv \frac{D_+(a)}{a}, \quad (1.2)$$

$$\Omega_k(a) \equiv \frac{\Omega_k H_0^2}{a^2 H^2(a)}, \quad (1.3)$$

$$\Omega_{DE}(a) \equiv \frac{\Omega_{DE} H_0^2}{a^{3[1+w_{\text{eff}}(a)]} H^2(a)}, \quad (1.4)$$

$$w_{\text{eff}}(a) \equiv \frac{1}{\ln a} \int_0^{\ln a} d \ln a' w(a'). \quad (1.5)$$

As we see in the eq. (1.1), growth rate has an explicit dependence on the dark energy equation of state. Therefore, by measuring the growth rate, one can obtain the information about the dark energy, thereby, the nature of accelerated expansion of the universe.

Predictions for the growth rate from different theories of gravity and the nature of dark energy can be well parametrized in the simple form of $f(z) = \Omega_m(z)^\gamma$. For example, $\gamma = 4/7$ for a Λ CDM model [11, 29], where the cosmological constant plays the role of observed accelerated expansion of the universe, and $\gamma = 0.68$ for the DGP model of modifications of gravity [23]. Thus, it is crucial to measure $f(z)$ from a given galaxy power spectrum to observationally unveil the nature of this mysterious component of the universe. Although a galaxy power spectrum gives a way to measure $f(z)$ at different redshifts, due to the vast parameter space allowed, an accurate measurement of $f(z)$ from a galaxy power spectrum alone is difficult [38]. Especially, when we use the redshift space galaxy power spectrum to the linear order, it is inevitable to have the growth rate, $f(z)$, be degenerate with a linear galaxy bias, b_L , such that $P_g^s(k, \mu) = P_m(k, \mu)(1 + \beta\mu^2)^2$, where $\beta(z) \equiv f(z)/b_L$ [16]. Thus, it is important to have an alternative method to measure the growth rate in addition to a redshift space galaxy power spectrum. Here, we propose the shape of voids in the redshift space as a sensitive probe of linear growth rate, $f(z)$.

The shape of the voids in redshift space has been studied in literature [25, 33, 34]. According to their study, the void volume increases in the redshift space as its boundary is stretched along the line of sight by redshift space distortion. This elongation of the void volume in the redshift space is diametrically opposite to what would happen to the distribution of galaxies in overdense regions, due to a reversed sign of the equation of motion sourced by local density field [14] (i.e., $\delta > 0$ for over dense regions and $\delta < 0$ for voids). Schmidt et al. [35] studied the effect of redshift space distortion on the void probability function (VPF). The VPF is a measure of probability, $P_0(V)$, that a randomly placed sphere of volume V contains no galaxy within [41]. For a given void in the real space, redshift space distortion stretches the void along the line of sight, increasing the volume of voids; thus, VPF, $P_0(V)$, increases toward a larger V .

Here, we study the *ellipticity* of voids in the redshift space as a probe of the linear growth rate, $f(z)$. Specifically, we shall use the ellipticity probability distribution function of Park & Lee [27] (hereafter, PL07) and Lee & Park [21]. PL07 proposed a void ellipticity distribution function as a sensitive probe of cosmology, noting that the shapes of voids are modulated by the competition between the tidal distortion and the cosmic expansion. Their model is based on the assumption that the underlying tidal field can be well described by the Zel'dovich approximation. They tested the model against the results from the Millennium simulations [39], finding a good agreement.

In practice, defining a void from a distribution of galaxies is non-trivial, as the definition of a void differs from one void finding algorithm to another (Colberg et al. [4] and references there in). Regardless of the ambiguity in the exact definition and the boundary shape of a void, the method of PL07 gives a robust measurement of ellipticities of voids (i.e., defined as space around local density minima): it uses the distribution of galaxies inside a void as a tracer of the underlying shape of the tidal field. Void statistics have been studied both in simulations and galaxy redshift surveys [8, 12, 26, 28]. With the abundant data of the galaxy redshift survey available from on-going and future galaxy surveys, properties of voids can be better understood. Furthermore, voids found from these surveys will provide a unique way to probe the history of the structure formation, and henceforth, the nature of dark energy.

Throughout this paper we use the maximum likelihood cosmological parameters of Komatsu et al. [18] (WMAP+BAO+SN of Table 1).

The goal of this paper is to provide an analytic insight into the observed ellipticities of voids, and establish basis for their application to cosmology. In § 2, we briefly review notations and definitions used in PL07 for a real space void ellipticity probability distribution function. In § 3, we study the effect of linear galaxy bias on the void ellipticity PDF. In § 4, we study the effect of redshift space distortion on the shape and ellipticity of observed voids. In § 5, we study the effect of the Poisson noise on the void ellipticity PDF, which arises as a consequence of tracing a void shape by a limited number of field galaxies inside the void. We also show that this Poisson noise can be the biggest limitation on the use of PL07 method for voids with a small number of field galaxies inside. In § 6, we compare the analytic prescriptions derived in the previous sections against the void ellipticity PDF extracted from the galaxy catalog of the Millennium simulation. Finally, our conclusions are in § 7.

2 Void in the real space

In this section, we briefly review the method of PL07. First, voids are extracted from a given galaxy distribution using a given void finding algorithm. We then find the ellipticities of voids, and construct a void ellipticity distribution function.

For each detected void, we define void galaxies, which reside inside a void, and calculate the inertia tensor of equal weight using N_{vg} void galaxies,

$$I_{ij}^r \equiv \sum_{\alpha=1}^{N_{\text{vg}}} x_{i,\alpha}^r x_{j,\alpha}^r, \quad (2.1)$$

where x_i is the distance from the center of a void (i.e., the mean, \bar{x}_i , has been removed). Suppose that lengths of the semiaxis of the best-fit ellipsoid to a void are p_1 , p_2 and p_3 , ordered as $p_1 \geq p_2 \geq p_3 \geq 0$. Then, one finds that they are proportional to the square root of the eigenvalues of the inertia tensor, I_1 , I_2 and I_3 , ordered as $I_1 \geq I_2 \geq I_3 \geq 0$. This motivates our defining the ellipticity of a void such that,

$$\begin{aligned} \epsilon &\equiv 1 - \frac{p_3}{p_1} = 1 - \sqrt{\frac{I_3}{I_1}} \\ \eta &\equiv 1 - \frac{p_2}{p_1} = 1 - \sqrt{\frac{I_2}{I_1}}. \end{aligned} \quad (2.2)$$

For a fixed volume of an ellipsoid, $V = \frac{4\pi}{3}p_1p_2p_3$, we can exhaust all the possible shapes of the ellipsoid in terms of ϵ and η . Figure 1 shows five special configurations of ellipsoids

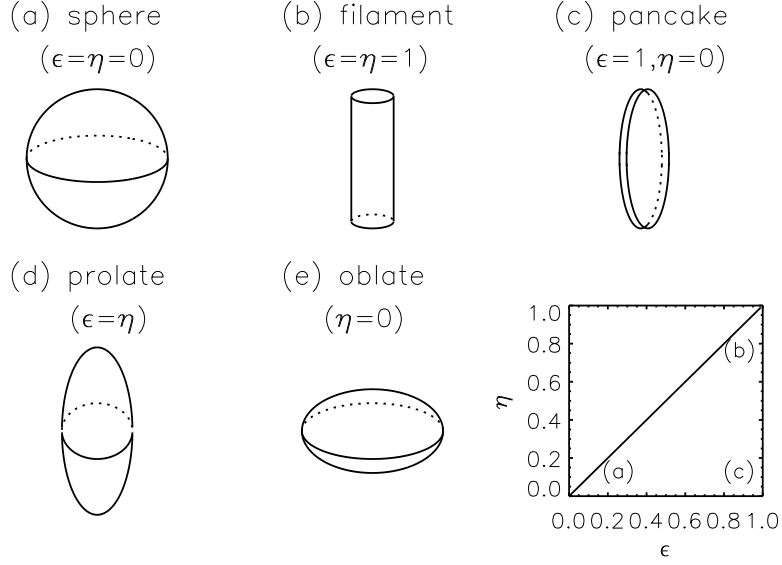


Figure 1. We show five special configurations of ellipsoids: (a) sphere, (b) filament, (c) pancake, (d) prolate spheroid and (e) oblate spheroid. In a plane of $\epsilon - \eta$, the lower triangle shows the possible configurations of ellipsoid, where each corner corresponds to a special configuration such as a sphere (lower left), a filament (upper right) and a pancake (lower right). Genuine triaxial ellipsoids are located in the middle of the triangle.

on the $\epsilon - \eta$ plane. Note that according to our definition (i.e., $p_1 \geq p_2 \geq p_3 \geq 0$), we have $0 \leq \eta \leq \epsilon \leq 1$.

- (a) For $\epsilon = \eta = 0$ (i.e., $p_1 = p_2 = p_3$), we have a spherical void.
- (b) For $\epsilon = \eta = 1$ (i.e., $p_1 \gg p_2 = p_3 = 0$), we have a filamentary void.
- (c) For $\epsilon = 1$ and $\eta = 0$ (i.e., $p_1 = p_2 \gg p_3 = 0$), we have a pancake void.
- (d) For $\epsilon = \eta$ (i.e., $p_1 > p_2 = p_3$), we have a prolate spheroid.
- (e) For $\eta = 0$ (i.e., $p_1 = p_2 > p_3$), we have an oblate spheroid.

We define the triaxiality parameter following Franx et al. [9],

$$T \equiv \frac{p_1^2 - p_2^2}{p_1^2 - p_3^2} = \frac{\eta(2 - \eta)}{\epsilon(2 - \epsilon)}, \quad (2.3)$$

and further divide the triaxial ellipsoid into two categories: prolate ellipsoids ($T > 0.5$) and oblate ellipsoids ($T < 0.5$).

2.1 Real-Space Ellipticity PDF

Here, we calculate the ellipticity probability distribution function of PL07 based on the unconditional joint probability density distribution of eigenvalues of a tidal tensor, $\{\lambda_1, \lambda_2, \lambda_3\}$ [7].

An unconditional PDF is given by

$$p(\lambda_1, \lambda_2, \lambda_3; \sigma_{R_L}) = \frac{3375}{8\sqrt{5}\pi\sigma_{R_L}^6} \exp\left(-\frac{3K_1^2}{2\sigma_{R_L}^2} + \frac{15K_2}{2\sigma_{R_L}^2}\right) \times (\lambda_1 - \lambda_2)(\lambda_2 - \lambda_3)(\lambda_1 - \lambda_3), \quad (2.4)$$

where $K_1 \equiv \lambda_1 + \lambda_2 + \lambda_3$, $K_2 \equiv \lambda_1\lambda_2 + \lambda_2\lambda_3 + \lambda_1\lambda_3$, and σ_{R_L} is the rms density fluctuation smoothed at the Lagrangean void size, R_L , with a top-hat window function, $W(kR_L)$,

$$\sigma_{R_L}^2 \equiv \int_{-\infty}^{\infty} \Delta^2(k) W^2(kR_L) d \ln k. \quad (2.5)$$

Here, we calculate $\Delta^2(k) \equiv \frac{k^3 P(k)}{2\pi^2}$ with a linear Boltzmann code, CAMB [22], with the best-fit cosmological parameters of WMAP+BAO+SN [18].

We derive a Lagrangean void size, R_L , from conservation of the number density within the volume elements of Eulerian and Lagrangean space,

$$n(\mathbf{x}, z) d^3x = \bar{n} d^3q, \quad (2.6)$$

where $n(\mathbf{x}, z) = \bar{n}(1 + \delta(\mathbf{x}, z))$ is a real-space comoving number density of matter, \bar{n} is a mean comoving number density, and \mathbf{x} and \mathbf{q} are Eulerian and Lagrangean coordinates, respectively. Therefore, we have

$$R_L(\mathbf{q}, z) = R_E(\mathbf{x}, z)(1 + \delta(\mathbf{x}, z))^{1/3}, \quad (2.7)$$

where R_E is an Eulerian size of void. PL07 derived the conditional PDF of $\{\lambda_1, \lambda_2\}$ for a given density contrast, $\delta = \sum_{i=1}^3 \lambda_i$ as follows,

$$p(\lambda_1, \lambda_2 | \delta, \sigma_{R_L}) = \frac{3375}{\sqrt{5}\pi\sigma_{R_L}^5} \times \exp\left[-\frac{5\delta^2}{2\sigma_{R_L}^2} \left(1 - \frac{3(\lambda_1 + \lambda_2)}{\delta} + \frac{3(\lambda_1^2 + \lambda_1\lambda_2 + \lambda_2^2)}{\delta^2}\right)\right] \times (2\lambda_1 + \lambda_2 - \delta)(\lambda_1 - \lambda_2)(\lambda_1 + 2\lambda_2 - \delta). \quad (2.8)$$

Here, as studied by Lavaux & Wandelt [19], signs of eigenvalues, λ_i tell us whether the void is spatially expanding or contracting along the corresponding semi-axes. In our notation, a given void spatially expands when $\lambda_i < 0$, and contracts when $\lambda_i > 0$. Here, we only consider three dimensionally expanding genuine voids, $0 > \lambda_1 \geq \lambda_2 \geq \lambda_3$ and $\delta = \sum_{i=1}^3 \lambda_i < 0$.

Now, under the premise of the strong correlation between the void shape, I_{ij} , and the underlying tidal tensor, $T_{ij} \equiv \frac{\partial^2 \Phi(\mathbf{q})}{\partial q_i \partial q_j}$, we have the following relations between the semimajor axis length, p_i , and the eigenvalues of the tidal tensor, λ_i :

$$\mu \equiv \frac{p_2}{p_1} = \left(\frac{1 - \lambda_2}{1 - \lambda_3}\right)^{1/2}, \quad (2.9)$$

$$\nu \equiv \frac{p_3}{p_1} = \left(\frac{1 - \lambda_1}{1 - \lambda_3}\right)^{1/2}, \quad (2.10)$$

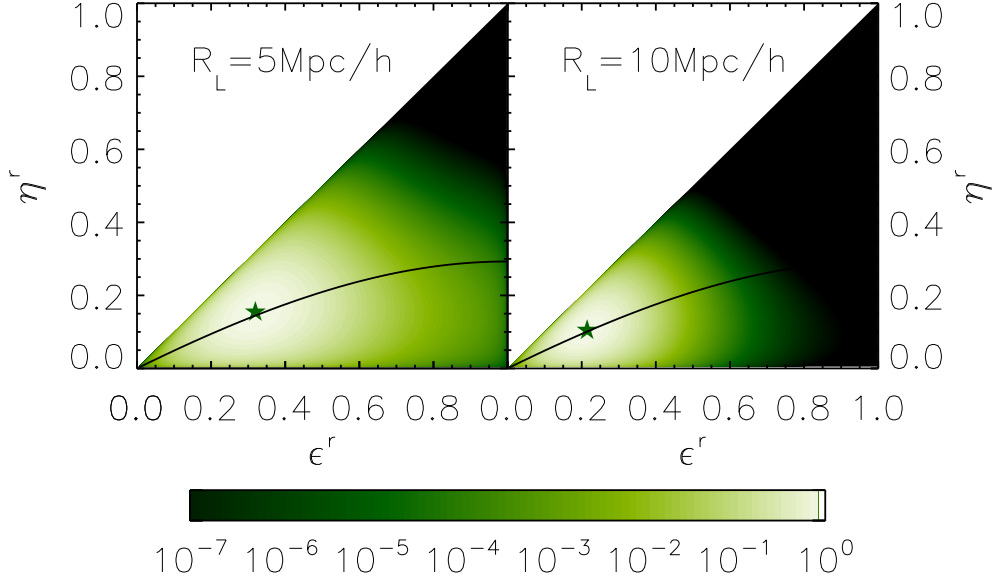


Figure 2. We show the ellipticity PDF for $R_L = 5$ and $10 h^{-1} \text{Mpc}$ at $z = 0$. PDF is normalized so that the peak values are 1. Solid lines show $T = 0.5$ and stars show the peaks of each PDF.

where we assume $\lambda_1 \geq \lambda_2 \geq \lambda_3$. Using these, one can define the PDF of ϵ and η as

$$p(\epsilon, \eta | \delta, \sigma_{R_L}) = p(\lambda_1(\mu, \nu), \lambda_2(\mu, \nu) | \delta, \sigma_{R_L}) \times \frac{4(\delta - 3)^2 \mu \nu}{(\mu^2 + \nu^2 + 1)^3}, \quad (2.11)$$

where $\mu = 1 - \eta$ and $\nu = 1 - \epsilon$, and

$$\lambda_1(\mu, \nu) = \frac{1 + (\delta - 2)\nu^2 + \mu^2}{\mu^2 + \nu^2 + 1} \quad (2.12)$$

$$\lambda_2(\mu, \nu) = \frac{1 + (\delta - 2)\mu^2 + \nu^2}{\mu^2 + \nu^2 + 1}. \quad (2.13)$$

From eq. (2.4), we see that the probability of having two of the three eigenvalues, λ_i , being equal is suppressed due to the last three factors (i.e., $(\lambda_1 - \lambda_2)(\lambda_2 - \lambda_3)(\lambda_1 - \lambda_3)$). Therefore, we have small probabilities of having ellipsoids with special configurations such as $\epsilon = \eta$ (prolate spheroids), $\eta = 0$ (oblate spheroids) and $\epsilon = 0$ (sphere): these special configurations correspond to $\lambda_1 = \lambda_2$, $\lambda_2 = \lambda_3$ and $\lambda_1 = \lambda_3$, respectively. In figure 2, we plot the ellipticity PDF of eq. (2.11) for $R_L = 5$ (left) and $10 h^{-1} \text{Mpc}$ (right), where $\delta_v = -0.9$. PDF is normalized so that the peak value is unity (stars). Note that for a fixed density contrast, δ , the exponential factor in eq. (2.4) is maximized when $\lambda_1 = \lambda_2 = \lambda_3$ allowing nearly spherical voids to have a finite probability.

We also plot the line separating the prolate and oblate ellipsoids (i.e., $T = 0.5$) (solid line). We see that locations of the ellipticity PDF peaks lie roughly on the line of $T = 0.5$, and PDF shifts toward smaller ellipticity both in ϵ and η for larger voids (i.e., smaller σ_{R_L} for a fixed set of cosmological parameters).

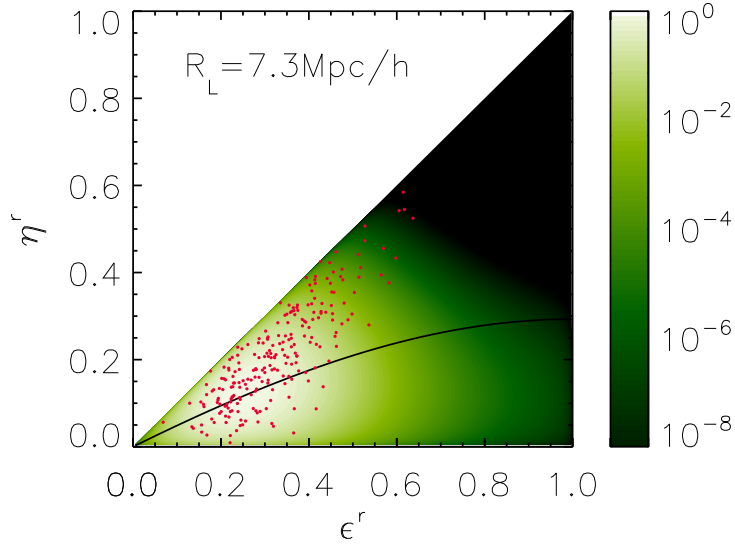


Figure 3. We show the 232 identified voids from the SDSS DR5 based on the catalog of Foster & Nelson [8], and the corresponding ellipticity PDF. From the catalog, we find $\bar{\epsilon} = 0.33$, $\bar{\eta} = 0.21$, $\bar{T} = 0.68$, $\bar{\delta}_v = -0.97$, $\bar{z} = 0.11$ and $R_L = 7.3h^{-1}\text{Mpc}$. PDF is normalized so that the peak values are 1, and the solid line shows $T = 0.5$. Note that the PDF is drawn only as a reference, and we do not correct for bias and redshift space distortion.

Also note that the ellipticity PDF in the real space has almost no preference for prolate or oblate ellipsoids ($T \simeq 0.5$). For $R_L = 5h\text{Mpc}^{-1}$, $\delta = -0.9$ and $z = 0$, we have mean ellipticities, $\bar{\epsilon}$ and $\bar{\eta}$ as follows,

$$\bar{\epsilon} = \int_0^1 d\epsilon \int_0^{\epsilon/2} d\eta \epsilon p(\epsilon, \eta | \delta, \sigma_{R_L}) = 0.37, \quad (2.14)$$

$$\bar{\eta} = \int_0^1 d\epsilon \int_0^{\epsilon/2} d\eta \eta p(\epsilon, \eta | \delta, \sigma_{R_L}) = 0.16, \quad (2.15)$$

$$\bar{T} = \int_0^1 d\epsilon \int_0^{\epsilon/2} d\eta T(\epsilon, \eta) p(\epsilon, \eta | \delta, \sigma_{R_L}) = 0.50, \quad (2.16)$$

and for $R_L = 1h\text{Mpc}^{-1}$, $\delta = -0.9$ and $z = 0$, we have $\bar{\epsilon} = 0.62$, $\bar{\eta} = 0.27$ and $\bar{T} = 0.55$.

However, previous observations and numerical studies indicate a preference for prolate ellipsoids. From voids detected in a ΛCDM N-body simulation, Platen et al. [31] claimed the axis ratio of best-fit ellipsoids to be 1 : 0.7 : 0.5 (i.e., $\epsilon = 0.5$, $\eta = 0.3$ and $T = 0.68$), and FN09 also found a preference for the prolate ellipsoids from the voids detected in the SDSS DR5 with $\epsilon = 0.33$, $\eta = 0.21$ and $\bar{T} = 0.66$. In figure 3, we show the distribution of ellipticities of 232 voids from the SDSS DR5 based on the catalog of Foster & Nelson [8]. We also show the corresponding ellipticity PDF just as a reference. The volume limited sample has a total of 52281 galaxies in a volume of $0.021h^{-3}\text{Gpc}^3$ ($\bar{n}_g \simeq 2.45 \times 10^{-3}h\text{Mpc}^{-3}$). In the ϵ - η plane, we clearly see the dominance of prolate voids, while analytic PDF has a slight to no preference of prolateness in the shape of voids. We think that the difference arises from the way we calculate ellipticities of voids. Earlier works extracted void shapes by calculating the shape tensor from volume elements inside detected voids. In this way, an extracted ellipticity

is sensitive to the boundary shape of the void as defined from a given void finder. Since a boundary is defined from galaxies in an overdense region, $\delta \gtrsim 0$, the tidal field around the boundary is subject to a stronger distortion from the external gravitational force. An unconditional ellipticity PDF of Doroshkevich [7], on the other hand, describes a tidal field at and around the density minima. Therefore, when we compare the analytic ellipticity PDF of PL07 against that of a simulation or galaxy survey, it is important to know whether the extracted ellipticity truly represents the shape of the tidal field around density minima.

3 Linear Galaxy Bias in the Real-Space Void ellipticity PDF

In the previous section, we have related the ellipticity PDF of voids to the tidal field generated by the matter density distributions. However, in reality, we obtain a void ellipticity PDF from a given galaxy distribution. In order to deduce the underlying matter density field, δ_m , from galaxy distributions, we use the well known linear galaxy bias, b_L , such that $\delta_v = b_L \delta_m$. Here, δ_v represents the density contrast of a void calculated from the number density of galaxies within the void, n_{vg} , and that of the cosmic mean, \bar{n}_g , (i.e, average number density of galaxies in a survey volume),

$$\delta_v \equiv \frac{n_{vg} - \bar{n}_g}{\bar{n}_g}. \quad (3.1)$$

Since the unconditional PDF of Doroshkevich [7] gives eigenvalues of tidal tensor, T_{ij} , generated by the matter density field, we use $\delta_m = \delta_v/b_L$ in Eqs.(2.8) \sim (2.13), where b_L is a linear galaxy bias to be calibrated from an observed ellipticity PDF. The filtering scale, R_L^m , should also be calculated following the definition of the linear bias,

$$R_L^m = R_E^m (1 + \delta_v/b_L)^{1/3}. \quad (3.2)$$

Here, an Eulerian size of void traced by the matter density field, R_E^m , is not a direct observable in a galaxy survey (i.e., the void size measured by the galaxy distribution, R_E^v , is a direct observable). Patiri et al. [28] showed that the radial density profiles of voids defined from dark matter and halo distribution of N-body simulations have similar shapes, and at large radii, haloes trace the dark matter. Based on this result, we set $R_E^m \simeq R_E^v$ here, and have

$$R_L^m = R_E^v (1 + \delta_v/b_L)^{1/3}. \quad (3.3)$$

Figure 4 shows the effect of linear galaxy bias on the real space ellipticity PDF both in 1-D (*bottom right*) and in 2-D (*top left to bottom left*). We normalize the 2-D PDFs to their peak values, and set the parameters to $R_L = 5h^{-1}\text{Mpc}$, $\delta_v = -0.9$ and $z = 0$. In the 1-D plot, we have PDF for four different linear galaxy biases, $b_L = 1.0$ (solid), 1.1(dotted), 2.0 (dashed) and 5.0 (dot-dashed), and in the 2-D plots, we have $b_L = 1.0$ (top left), 1.1 (top right) and 2.0 (bottom left).

In the 2-D plots, the solid lines show $T = 0.5$, and the stars show the peaks of each PDF. Regardless of the values of bias, peaks of PDF lie on the solid lines ($T = 0.5$), and the ratio of prolate to oblate spheroids is ~ 0.5 as in the case of unbiased (i.e., $b_L = 1$) ellipticity PDF.

We clearly see an effect of bias on the void PDF as we increase the galaxy bias b_L from its unbiased value, $b_L = 1$, to biased value, $b_L > 1$. As we increase the bias from $b_L = 1$, the ellipticity PDF peaks at smaller ellipticities more sharply. For $b_L > 2.0$, the shape of

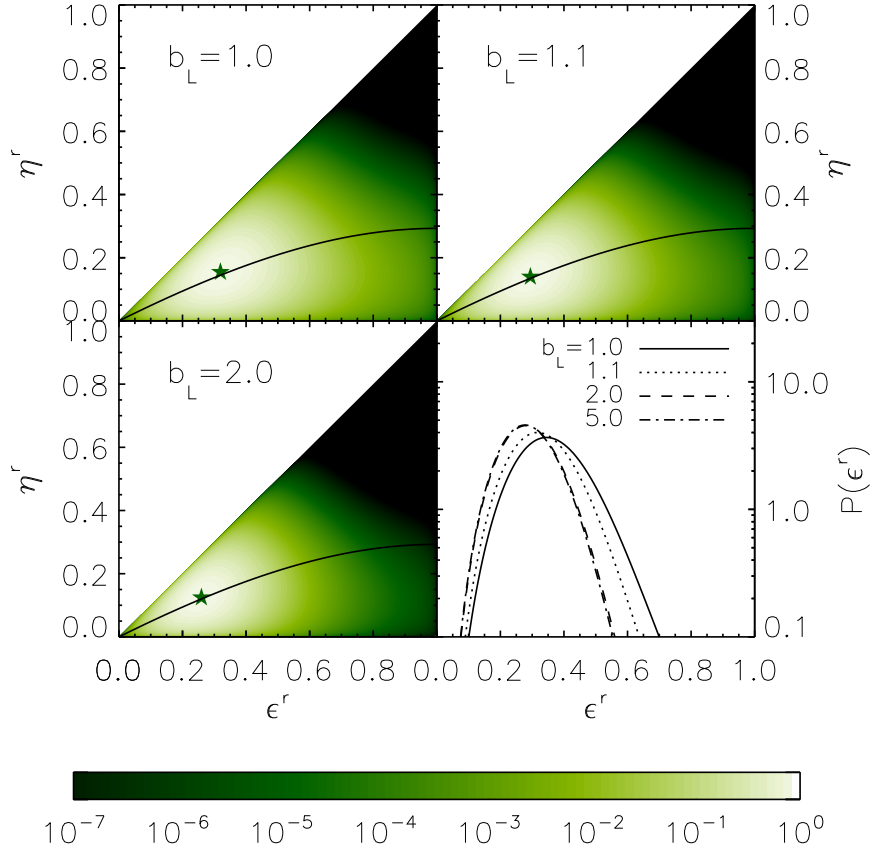


Figure 4. In this figure, we show the effect of linear galaxy bias on the real space void ellipticity PDF both in 1-D (*bottom right*) and 2-D (*top left to bottom left*). The 2-D PDFs are normalized so that the peak values are 1. In the 1-D plot, we have PDF for four different biases, $b_L = 1.0$ (solid), 1.1 (dotted), 2.0 (dashed) and 5.0 (dot-dashed). In the 2-D plots, the solid lines show $T = 0.5$, and the stars show the peaks of each PDF. Here, we have used $R_L = 5h^{-1}\text{Mpc}$, $\delta_v = -0.9$ and $z = 0$.

PDF converges quickly, and becomes insensitive to the further change in b_L . As a larger bias reduces the matter density contrast, δ_m , for a fixed value of δ_v , a smaller matter density contrast yields a less pronounced tidal field around the density minima, yielding smaller ellipticity.

In Eqs.(2.8) \sim (2.13), we see the effect of bias through σ_{R_L} . Since the Lagrangean size of void, R_L^m , (as defined in eq. (3.3)) sets the smoothing scale of the density field for calculating σ_{R_L} , the larger the R_L^m is, the smaller the σ_{R_L} becomes. Again, a smaller rms fluctuation of the matter density field leads to a weaker tidal field, and hence, the smaller ellipticity of the void. We see that, although the linear bias, b_L , and σ_8 , which is directly proportional to the σ_{R_L} , are nearly degenerate in the parameter space of the biased ellipticity PDF, their correlation is directly opposite in the case of the galaxy power spectrum, $P_g(k) \propto b_L^2 \sigma_8^2$. This feature of the biased void ellipticity PDF allows us to better constrain both the linear bias, b_L , and the rms density fluctuations, σ_8 , when combined with the galaxy power spectrum.

4 Void in the redshift space

In order to compare the analytic and observed ellipticity PDFs, we need to understand the effect of the redshift space distortion on the ellipticity of a given void. Unlike galaxies and galaxy clusters, which reside in density maxima, voids reside in density minima, where the diverging velocity field pushes the boundary and the field galaxies inside the voids outward, expanding their volume in all directions [14].

A real-space inertia tensor is defined in eq. (2.1), and that of the redshift-space is similarly defined as

$$I_{ij}^s \equiv \sum_{\alpha=1}^{N_{\text{vg}}} x_{\alpha,i}^s x_{\alpha,j}^s, \quad (4.1)$$

where N_{vg} is the number of void galaxies, and \mathbf{x}_{α}^s is the redshift-space position of an α -th void galaxy. An inertia tensor is symmetric by definition (i.e., $I_{ij} = I_{ji}$), and traces a shape of a void from an underlying void galaxy distribution. Park & Lee [27] identified voids from the Millennium simulation using the void finding algorithm of Hoyle & Vogeley [12], and extracted the ellipticity PDF of voids using the inertia tensor using void galaxies as tracers. They found that the distribution of ellipticities of voids from the Millennium simulation follows that of linear theory (Zel'dovich Approximation) prediction in real space.

Here, we study the effect of the redshift space distortion on the ellipticity PDF. First, we calculate the redshift space inertia tensor as follows.

A mapping between the real-space and the redshift space is given by

$$x_1^s = x_1^r \quad (4.2)$$

$$x_2^s = x_2^r \quad (4.3)$$

$$x_3^s = x_3^r - f \mathbf{u} \cdot \hat{\mathbf{x}}_3^r, \quad (4.4)$$

where $f \equiv \frac{d \ln \delta(a)}{d \ln a}$ is the growth rate, and the unit vector, $\hat{\mathbf{x}}_3^r$, is along the line of sight. Here, $\mathbf{u} \equiv \frac{\mathbf{v}}{\mathcal{H}f}$, where \mathbf{v} is the peculiar velocity of a void galaxy, and $\mathcal{H}(a) = aH(a)$ is a comoving Hubble rate.

We define $\kappa(\mathbf{x}^r)$ to quantify the strength of the redshift space distortion as

$$\kappa(\mathbf{x}^r) \equiv -\frac{f \hat{\mathbf{x}}_3^r \cdot \mathbf{u}(\mathbf{x}^r)}{x_3^r}. \quad (4.5)$$

With $\kappa(\mathbf{x}^r)$, we re-write eq. (4.4) as

$$x_3^s = x_3^r (1 + \kappa(\mathbf{x}^r)), \quad (4.6)$$

and we relate the redshift-space inertia tensor to the real-space inertia tensor as follows,

$$I_{11}^s = I_{11}^r \quad (4.7)$$

$$I_{12}^s = I_{12}^r \quad (4.8)$$

$$I_{22}^s = I_{22}^r \quad (4.9)$$

$$I_{13}^s = I_{13}^r + \sum_{\alpha=1}^{N_{\text{vg}}} x_{\alpha,1}^r x_{\alpha,3}^r \kappa_{\alpha} \quad (4.10)$$

$$I_{23}^s = I_{23}^r + \sum_{\alpha=1}^{N_{\text{vg}}} x_{\alpha,2}^r x_{\alpha,3}^r \kappa_{\alpha} \quad (4.11)$$

$$I_{33}^s = I_{33}^r + 2 \sum_{\alpha=1}^{N_{\text{vg}}} x_{\alpha,3}^r x_{\alpha,3}^r \kappa_{\alpha} + \sum_{\alpha=1}^{N_{\text{vg}}} x_{\alpha,3}^r x_{\alpha,3}^r \kappa_{\alpha}^2, \quad (4.12)$$

where

$$\kappa_{\alpha} = -\frac{f\mu_{\alpha}u_{\alpha}}{x_{\alpha,3}^r}, \quad (4.13)$$

and μ is the angle between the peculiar velocity, \mathbf{u} , and the line of sight (i.e., $\mu \equiv \hat{\mathbf{u}} \cdot \hat{\mathbf{x}}_3^r$).

Once we have the redshift space inertia tensor either numerically, from eq. (4.1), or analytically in terms of κ , from eqs. (4.7) ~ (4.12), we can calculate the ellipticity of a given void, ϵ and η , from eigenvalues of the redshift space inertia tensor, ($I_1^s \geq I_2^s \geq I_3^s$) as in eq. (2.2).

Since κ is a function of the peculiar velocity field, we can use linear theory to calculate κ for an arbitrary density field, $\delta(\mathbf{x}^r)$, as,

$$\begin{aligned} \kappa(\mathbf{x}^r) &\equiv -\frac{f\hat{\mathbf{x}}_3^r \cdot \mathbf{u}(\mathbf{x}^r)}{x_3^r} = -\frac{f\hat{\mathbf{x}}_3^r \cdot \nabla\Phi(\mathbf{x}^r)}{4\pi G a^2 \bar{\rho} x_3^r} \\ &= -\frac{f}{4\pi G a^2 \bar{\rho} x_3^r} \int \frac{d^3k}{(2\pi)^3} i\mathbf{k} \cdot \hat{\mathbf{x}}_3^r \tilde{\Phi}(\mathbf{k}) e^{i\mathbf{k} \cdot \mathbf{x}^r} \\ &= \frac{f}{x_3^r} \int \frac{d^3k}{(2\pi)^3} i\mathbf{k} \cdot \hat{\mathbf{x}}_3^r \frac{\tilde{\delta}(\mathbf{k})}{k^2} e^{i\mathbf{k} \cdot \mathbf{x}^r} \\ &= \frac{f}{x_3^r} \int_0^\infty \frac{dk}{(2\pi)^3} i k \int_0^{2\pi} d\phi_k \int_{-1}^1 d\mu_k \mu_k \tilde{\delta}(\mathbf{k}) e^{i\mathbf{k} \cdot \mathbf{x}^r}, \end{aligned} \quad (4.14)$$

where $\mu_k \equiv \cos\theta_k$. Here, we used the linear relation between a peculiar velocity and a gravitational field derived from Zel'dovich Approximation [13],

$$\mathbf{v} = -\frac{\mathcal{H}f}{4\pi G a^2 \bar{\rho}} \nabla\Phi, \quad (4.15)$$

and a Poisson equation,

$$\nabla^2\Phi = 4\pi G a^2 \bar{\rho} \delta. \quad (4.16)$$

We explicitly write a cosine angle between \mathbf{k} and \mathbf{x} , in a spherical coordinate as

$$\cos\gamma \equiv \cos\theta_k \cos\theta_x + \cos(\phi_k - \phi_x) \sin\theta_k \sin\theta_x, \quad (4.17)$$

where $\mathbf{k} \cdot \mathbf{x} = kx \cos \gamma$. Here, in order to calculate the effect of peculiar velocity on the void shape, we need to know the density profile of a void, $\delta(\mathbf{x})$ in the real space. Sheth & van de Weygaert [36] studied an evolution of a radial density profile of an isolated void, and found that the density profile evolves into an increasingly similar shape to a top-hat function. With N-body simulations both in sCDM and Λ CDM, Colberg et al. [3] found that the radial density profile of a void is universal, having $\rho(r < r_{\text{eff}})/\rho(r_{\text{eff}}) \propto \exp[(r/r_{\text{eff}})^\alpha]$, where r_{eff} is the effective radius of the void and $\alpha \sim 2$. These analytic radial density profiles are also seen in the voids identified from the galaxy distribution of the Sloan Digital Sky Survey as a sharp rise of density contrast near the boundary of the void [26, 28]. In this section, we approximate the radial density profile of the void, $\delta(r)$, to be a top-hat function for simplicity,

$$\delta(\mathbf{x}^r) = \begin{cases} \bar{\delta} & \text{within the void} \\ 0 & \text{outside the void} \end{cases}, \quad (4.18)$$

where $\bar{\delta}$ is the average density contrast within the void. We will discuss further about more general density profiles at the end of this section.

Below, we will show analytic solutions for the redshift space ellipticity for some of the limiting cases.

4.1 Spherical Void

First, we consider a sphere with zero real space ellipticity, $\epsilon^r = 0$ and $\eta^r = 0$, with three eigenvalues of the inertia tensor of $I_1^r = I_2^r = I_3^r$. For a spherical top hat density field, we have

$$\tilde{\delta}(\mathbf{k}) = 4\pi R^3 \bar{\delta} \frac{j_1(kR)}{kR}. \quad (4.19)$$

Therefore, eq. (4.14) becomes

$$\begin{aligned} \kappa(\mathbf{x}^r) &= \frac{4\pi R^3 f \bar{\delta}}{x_3^r} \int_0^\infty \frac{dk}{(2\pi)^3} i k \frac{j_1(kR)}{kR} \\ &\times \int_0^{2\pi} d\phi_k \int_{-1}^1 d\mu_k \mu_k e^{i\mathbf{k} \cdot \mathbf{x}^r}. \end{aligned} \quad (4.20)$$

We first integrate the angular portion of the integration, $\int d\Omega_k \mu_k e^{i\mathbf{k} \cdot \mathbf{x}^r}$, by expanding the exponent into Legendre polynomials,

$$e^{i\mathbf{k} \cdot \mathbf{x}^r} = \sum_l (-i)^l (2l+1) j_l(-kx) P_l(\cos \gamma), \quad (4.21)$$

and using the Spherical harmonics addition theorem (a.k.a., Legendre addition theorem). We find

$$\int d\Omega_k \mu_k e^{i\mathbf{k} \cdot \mathbf{x}^r} = 4\pi i j_1(kx) \cos \theta_x. \quad (4.22)$$

Finally, we obtain κ for a spherical void as

$$\begin{aligned} \kappa(\mathbf{x}^r) &= \frac{4\pi R^3 f \bar{\delta}}{x_3^r} \int_0^\infty \frac{dk}{(2\pi)^3} i k \frac{j_1(kR)}{kR} [4\pi i j_1(kx) \cos \theta_x] \\ &= -\frac{2R^2 f \bar{\delta} \cos \theta_x}{\pi x_3^r} \int_0^\infty dk j_1(kR) j_1(kx) \\ &= -\frac{2R^2 f \bar{\delta} \cos \theta_x}{\pi x_3^r} \left(\frac{\pi x}{6R^2} \right) = -\frac{f \bar{\delta}}{3}. \end{aligned} \quad (4.23)$$

As we see from eq. (4.23), κ is independent of positions in the void, and therefore the three eigenvalues of the redshift space inertia tensor for a redshift space void, $I_1^s \geq I_2^s \geq I_3^s$, are

$$I_1^s = I_1^r(1 + \kappa)^2 \quad (4.24)$$

$$I_2^s = I_2^r \quad (4.25)$$

$$I_3^s = I_3^r, \quad (4.26)$$

and the ellipticity, ϵ and η are

$$\epsilon^s = \eta^s = 1 - \frac{1}{1 + \kappa} = 1 - \frac{1}{1 - f\bar{\delta}/3}, \quad (4.27)$$

following eq. (2.2). Now, the linear growth rate, $f \equiv \frac{d \ln D(a)}{d \ln a}$, for the Λ CDM model is approximately given as [11, 29],

$$f(z) = \Omega(z)^{4/7}, \quad (4.28)$$

where

$$\Omega(z) = \frac{\Omega_m(1+z)^3}{\Omega_m(1+z)^3 + \Omega_\Lambda}. \quad (4.29)$$

For $\Omega_m = 0.25$ and $\Omega_\Lambda = 0.75$, $f \simeq 0.5$ at $z = 0$, and thus, for a spherical void with an average density contrast of $\bar{\delta} = -0.9$, we have $\epsilon^s = \eta^s \simeq 0.13$. Since there is no special orientation for a spherical void, any void with sufficiently small real space ellipticity, $\epsilon^r \sim \eta^r \sim 0$, becomes a prolate ellipsoid (i.e., $\epsilon^s \sim \eta^s \neq 0$) in the redshift space with its ellipticity given by eq. (4.27).

4.2 Spheroidal Void

When two of the three lengths of the semiaxis are equal, we have a spheroidal void. We set the direction of the longest and shortest semiaxis to be along the line of sight for prolate and oblate spheroids respectively. As in the spherical void, we assume a spheroidal top hat density contrast and solve eq. (4.14) to have κ to the first order in ϵ^r ,

$$\kappa(\mathbf{x}^r) \simeq -\frac{f\bar{\delta}}{3}(1 \mp 2\epsilon^r,) \quad (4.30)$$

where “−” and “+” signs are for prolate and oblate spheroids respectively. Here, we set the longest axis along the line of sight for prolate spheroids, and set the shortest axis along the line of sight for oblate spheroids. We compared the analytic prediction against numerical calculations, and found that

$$\kappa(\mathbf{x}^r) \simeq -\frac{f\bar{\delta}}{3}(1 \mp \epsilon^r,) \quad (4.31)$$

fits the result better. For each case, we have redshift space ellipticity as a function of real space ellipticity and κ as follows,

$$\epsilon^s = 1 - \frac{1 - \epsilon^r}{1 + \kappa}, \quad (4.32)$$

$$\epsilon^s = 1 - (1 - \epsilon^r)(1 + \kappa). \quad (4.33)$$

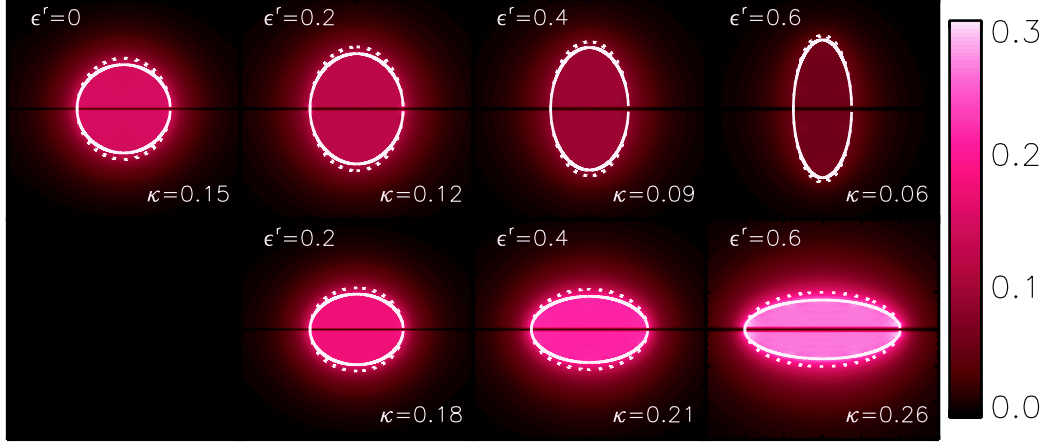


Figure 5. We show the spatial distribution of the value of $\kappa(\mathbf{x}^r)$ in x-z plane for prolate spheroids with its longest axis along the line of sight (*top*), and oblate ellipsoids with its shortest axis along the line of sight (*bottom*) for different real space ellipticities, ϵ^r . We also plot real space (solid lines) and redshift space (dotted lines) shapes of voids. Here, we use $f = 0.5$ and $\delta = -0.9$.

In contrast to the spherical void, whose redshift space ellipticity is always larger than that of real space, ellipticity of a spheroid either increases or decreases in the redshift space.

In figure 5, we show the result of numerical calculations for the spatial distribution of the value of $\kappa(\mathbf{x}^r)$ in the x-z plane for prolate spheroids with its longest axis along the line of sight (*top*), and oblate ellipsoids with its shortest axis along the line of sight (*bottom*) for different real space ellipticities, ϵ^r . In the figure, the center of the spheroids corresponds to the origin of the coordinate, and the x-z plane cuts the middle of the spheroid. We also plot the real space (solid lines) and redshift space (dotted lines) shapes of voids. Here, we use $f = 0.5$ and $\delta = -0.9$.

We see that the deformation of the void shape, $\kappa \propto u_3$, is the largest when the shortest semiaxis is along the line of sight due to the largest line-of-sight peculiar velocity. This result is in agreement with the earlier work of Icke [14]. When the longest semiaxis is along the line of sight (i.e., *top* figures), ellipticity only *increases* in the redshift space, while ellipticity only *decreases* when the shortest semiaxis is along the line of sight (i.e., *bottom* figures). For the spherical void, $\epsilon^r = 0$, we have $\epsilon^s = 0.13$ as expected from eq. (4.27). For prolate and oblate spheroids with $\epsilon^r = 0.2, 0.4$ and 0.6 , we have $\kappa = 0.12, 0.09$ and 0.06 , and $\kappa = 0.18, 0.21$ and 0.26 from the numerical calculations respectively. This is in a good agreement with the fitting function of eq. (4.31): for prolate and oblate spheroids with $\epsilon^r = 0.2, 0.4$ and 0.6 , eq. (4.31) yields $\kappa = 0.12, 0.09$ and 0.06 , and $\kappa = 0.18, 0.21$ and 0.24 , respectively.

Using Eqs.(4.33) and (4.33), for prolate and oblate spheroids with $\epsilon^r = 0.2, 0.4$ and 0.6 , we have redshift space ellipticities of $\epsilon^s = 0.29, 0.45$ and 0.62 , and $\epsilon^s = 0.06, 0.27$ and 0.50 respectively. In general, the fractional change in the ellipticity, $(\epsilon^s - \epsilon^r)/\epsilon^r$, becomes smaller for a larger ϵ^r .

Although we have constant κ here (i.e., independent of the position in the void), this is not true for arbitrarily oriented voids. In the case of tilted voids, $\kappa(\mathbf{x}^r)$ is a function of the real space coordinate, \mathbf{x}^r , and has both positive and negative values by definition, $\kappa(\mathbf{x}^r) \propto u_3/x_3$.

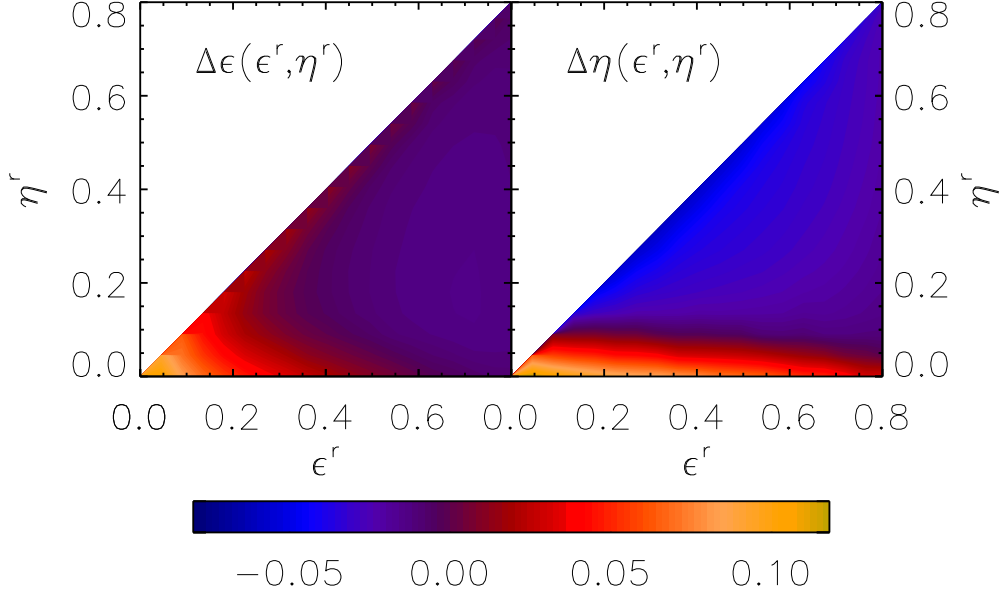


Figure 6. We show the effect of redshift space distortion on real space void ellipticities, ϵ^r and η^r . For a given set of ellipticities in real space, we plot the change in ellipticities, $\Delta\epsilon(\epsilon^r, \eta^r) \equiv \epsilon^s(\epsilon^r, \eta^r) - \epsilon^r$ (*left*) and $\Delta\eta(\epsilon^r, \eta^r) \equiv \eta^s(\epsilon^r, \eta^r) - \eta^r$ (*right*). Here, we have assumed a top-hat density profile with $\bar{\delta} = -0.9$ and $f = 0.5$.

4.3 Redshift-Space Ellipticity Distribution Function

For a given ellipticity in real space, the corresponding redshift-space ellipticity can either increase or decrease, depending on the real space shape and orientation of the void with respect to the line of sight, except for a spherical void, whose ellipticity can only increase. Here, we calculate changes in ellipticities for a given set of real space ellipticities, ϵ^r and η^r ,

$$\Delta\epsilon(\epsilon^r, \eta^r) \equiv \epsilon^s(\epsilon^r, \eta^r) - \epsilon^r \quad (4.34)$$

$$\Delta\eta(\epsilon^r, \eta^r) \equiv \eta^s(\epsilon^r, \eta^r) - \eta^r, \quad (4.35)$$

averaged over possible orientations. We numerically solve eq. (4.14) for $\kappa(\mathbf{x}^r)$, with a top-hat density contrast, $\delta(\mathbf{x}^r)$, and calculate the redshift-space ellipticity, ϵ^s and η^s , from the redshift-space inertial tensor, I_{ij}^s . In figure 6, we show $\Delta\epsilon(\epsilon^r, \eta^r)$ (*left*) and $\Delta\eta(\epsilon^r, \eta^r)$ (*right*) for $\bar{\delta} = -0.9$ and $f = 0.5$. As expected, a spherical void in the real space becomes a prolate spheroid (i.e., $\epsilon = \eta \neq 0$) in the redshift space with its ellipticity given by eq. (4.27). Also, we see a clear preference for positive $\Delta\epsilon$ for any triaxial void, especially at a small ϵ^r . As for $\Delta\eta$, spheroidal voids tend to be triaxial voids in the redshift space. From both $\Delta\epsilon$ and $\Delta\eta$, we find that an oblate void ($T < 0.5$) in real space tends to be a more prolate shape ($T > 0.5$) in the redshift space, and we have more prolate voids in redshift space ellipticity PDF.

In figure 7, we compare the ellipticity PDF of real space and redshift space for $R_L = 4h^{-1}\text{Mpc}$ (*top*) and $R_L = 9h^{-1}\text{Mpc}$ (*bottom*). Here, we use $b_L = 1$ and $\bar{\delta} = -0.9$, while varying the linear growth rate, f , from 0.5 to 1.5. We show the redshift space ellipticity PDF together with that of real space as a reference. Since the expansion rate of the void is

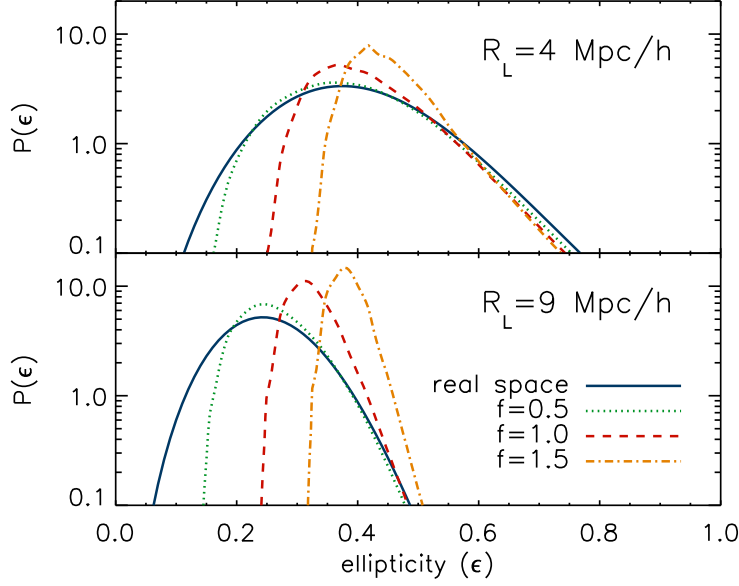


Figure 7. We compare the ellipticity PDF of real space and redshift space for $R_L = 4h^{-1}\text{Mpc}$ (*top*) and $R_L = 9h^{-1}\text{Mpc}$ (*bottom*). Here, we use $b_L = 1$ and $\bar{\delta} = -0.9$, while varying the linear growth rate: $f = 0.5$ (dotted), 1.0 (dashed) and 1.5 (dot-dashed). We also show the real space ellipticity PDF (solid) as a reference.

set by the matter density distribution inside the void, in linear theory, it is proportional to the linear growth rate. As the effect of the redshift space distortion on the ellipticity PDF is more prominent for a larger $f(z)$ and smaller ϵ^r , the redshift space ellipticity PDF becomes more skewed in shape with the mean ellipticity being higher than that of real space, $\bar{\epsilon}^s > \bar{\epsilon}^r$. Also note that the left tails of each redshift space ellipticity PDF approximately show the redshift space ellipticity, ϵ^s , of a spherical void, $\epsilon^r = 0$, and thus, we have

$$\epsilon^{\text{left}} \sim \epsilon^s(\epsilon^r = 0) = 1 - \frac{1}{1 - \frac{f\bar{\delta}}{3}}. \quad (4.36)$$

Therefore, in principle, with only the location of the left tail of PDF determined, we can put a constraint on $f\bar{\delta}$. This is a great benefit of using morphological information of structure, which is directly distorted in the redshift space. Although what we can actually measure is $f\bar{\delta} = \beta\bar{\delta}_v$, where $\beta \equiv f/b_L$, the entire shape of ellipticity PDF can lift the degeneracy between f and b_L . We can easily see this in the figure 4, where the increase in b_L decreases the mean ellipticity, $\bar{\epsilon}^r$, shifting the right tails of PDF toward lower ϵ^r , while the left tails are almost unaffected. Unlike a galaxy power spectrum, $P(k)$, which gives a constraint on the linear growth rate that is degenerate with the linear bias, $\beta \equiv f/b_L$, a void ellipticity PDF has a potential to constrain the linear growth rate separately from the other cosmological parameters. In other words, for a given galaxy survey, we have the situation in which we “*buy one, get one free*”.

4.4 Void With General Radial Density Profile

So far, we have derived the redshift space ellipticity PDF for the top-hat density contrast, $\delta(\mathbf{x})$; however, the realistic radial profile of void density contrast does not necessarily follow the top-hat shape. The main parameter controlling the shape of the redshift space ellipticity PDF is $\kappa(\mathbf{x}^r)$ as in eq. (4.14), and its value is given by $\kappa(\mathbf{x}^r) = A(\mathbf{x}^r)f\bar{\delta}$, where $A(\mathbf{x}^r)$ is solely determined by the density profile of a void (e.g., a void with a spherical top hat density profile has $A(\mathbf{x}^r) = -1/3$).

As an example, we parametrize the radial density profile of the void following the accumulated density profile of voids from the N-body simulation of Colberg et al. [3], $\rho(<r)/\rho(r_{\text{eff}}) \propto \exp[(r/r_{\text{eff}})^\alpha]$, where the density profile at a given radius, $\rho(r)$, is given as follows

$$\rho(r) \propto \exp \left[\left(\frac{r}{r_{\text{eff}}} \right)^\alpha \right] \left[1 + \frac{\alpha}{3} \left(\frac{r}{r_{\text{eff}}} \right)^\alpha \right]. \quad (4.37)$$

Here, instead of using the original form of Colberg et al. [3], we use an exponential density profile,

$$\delta(r) = \delta_0 \left(\frac{e^{[(r/r_{\text{eff}})^\alpha - 1]} - 1}{e^{-1} - 1} \right), \quad (4.38)$$

where we forced $\rho(r_{\text{eff}}) = \bar{\rho}$, at the effective radius, r_{eff} , (i.e., $\delta(r_{\text{eff}}) = 0$), and $\delta_0 \equiv \delta(r = 0)$. Figure 8 shows the profiles of the density contrast, $\delta(r)$, for top-hat (solid) and exponential profiles of eq. (4.38) with $\alpha = 1$ (dotted), 2 (dashed) and 4 (dot-dashed). Note that for a top-hat density contrast, we have $\bar{\delta} = \delta_0$, while for the exponential profiles, we have

$$\bar{\delta} = \frac{\int_0^{r_{\text{eff}}} r^2 \delta(r) dr}{\int_0^{r_{\text{eff}}} r^2 dr}, \quad (4.39)$$

where $\delta(r)$ is given as eq. (4.38). In figure 9, we show the redshift space ellipticity PDF for $f = 0.5$ (green), 1.0 (red) and 1.5 (orange) together with the real space ellipticity PDF (blue). Here, we use $R_L = 9h^{-1}\text{Mpc}$ and the radial density profile of the density contrast is set to be either a top-hat (solid), $\delta(r < R_{\text{void}}) = \bar{\delta}$, or an exponential (dotted) given by eq. (4.38) with $r_{\text{eff}} = R_{\text{void}}$ and $\alpha = 2$. We use $\delta_0 = -0.40$ and -0.82 for the top-hat density profile and the exponential profile, respectively, in order to keep the same mean density contrasts, $\bar{\delta} = -0.4$, for different density profiles. Here, we clearly see degeneracy between the shape of the potential and the linear growth rate, f . Therefore, a better understanding of the density profile of a void is required when constraining the linear growth rate from the redshift space ellipticity PDF.

5 Effect of Void Finding and Poisson Noise on the Void Ellipticity PDF

In the previous sections, we have shown how to incorporate the galaxy bias and redshift space distortion into the calculation of the ellipticity PDF. In this section, we investigate the biases and errors that arise when using the inertia tensor, I_{ij} , as an estimate of the void ellipticity. Since a void is a sparse region in a galaxy distribution, the number of galaxies inside a void, N_{vg} , is limited. Therefore the error in the ellipticity calculated from the inertia tensor of the void galaxy distribution is dominated by the Poisson statistics.

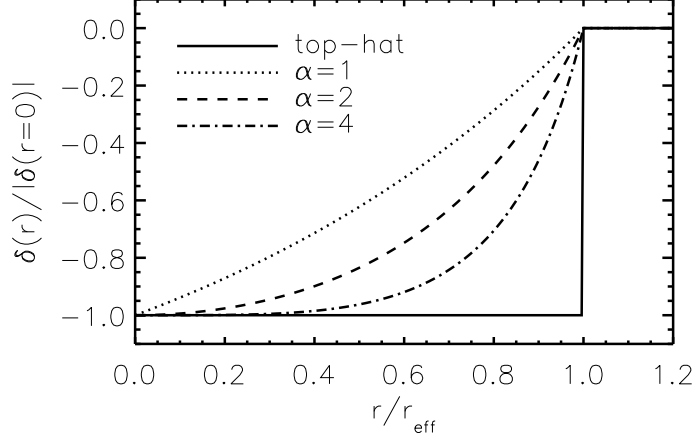


Figure 8. We show profiles of the density contrast, $\delta(r)$, for top-hat (solid) and exponential profiles of eq. (4.38) with $\alpha = 1$ (dotted), 2 (dashed) and 4 (dot-dashed). Here, we assumed that the density at the effective radius, r_{eff} , becomes that of the cosmic mean, $\rho(r_{\text{eff}}) = \bar{\rho}$, or, $\delta(r_{\text{eff}}) = 0$.

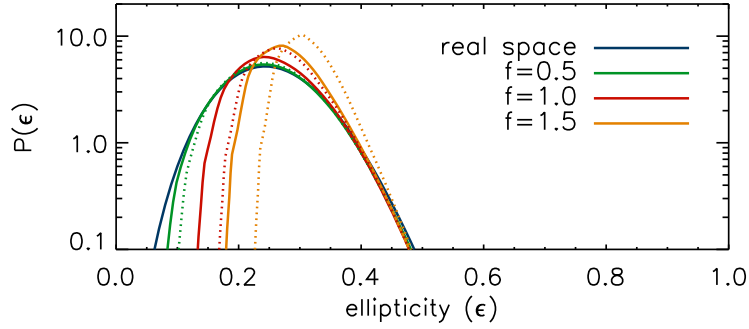


Figure 9. We show the redshift space ellipticity PDF for $f = 0.5$ (green), 1.0 (red) and 1.5 (orange) together with real space ellipticity PDF (blue). Here, we use $R_L = 9h^{-1}\text{Mpc}$. The radial density profile of density contrast is set to be either a top-hat (solid), $\delta(r < R_{\text{void}}) = \bar{\delta}$, or an exponential (dotted) as in eq. (4.38), with $r_{\text{eff}} = R_{\text{void}}$ and $\alpha = 2$. We use $\delta_0 = -0.40$ and -0.82 for the top-hat and the exponential density profile, respectively, in order to keep the same mean density contrasts, $\bar{\delta} = -0.4$, for different density profiles. Here, we see degeneracy between the shape of the potential and the linear growth rate, f .

Let us define two stochastic variables, x and y , as follows,

$$x \equiv \mu_x + \Delta x, \quad (5.1)$$

$$y \equiv \mu_y + \Delta y, \quad (5.2)$$

where μ_x and μ_y are the means of x and y , respectively, and $\langle \Delta x \rangle = \langle \Delta y \rangle = 0$. We have

variances and covariance defined as,

$$\sigma_x^2 \equiv \langle (x - \mu_x)^2 \rangle = \langle (\Delta x)^2 \rangle, \quad (5.3)$$

$$\sigma_y^2 \equiv \langle (y - \mu_y)^2 \rangle = \langle (\Delta y)^2 \rangle, \quad (5.4)$$

$$\sigma_{xy} \equiv \langle (x - \mu_x)(y - \mu_y) \rangle = \langle \Delta x \Delta y \rangle. \quad (5.5)$$

A mean of a rational is given by the following form,

$$\mu_{x/y} = \left\langle \frac{\mu_x + \Delta x}{\mu_y + \Delta y} \right\rangle. \quad (5.6)$$

Expanding Δy up to the second order, we have

$$\begin{aligned} \mu_{x/y} &\simeq \frac{\mu_x}{\mu_y} \left\langle \left[1 + \frac{\Delta x}{\mu_x} \right] \left[1 - \frac{\Delta y}{\mu_y} + \left(\frac{\Delta y}{\mu_y} \right)^2 \right] \right\rangle \\ &\simeq \frac{\mu_x}{\mu_y} \left(1 + \frac{\sigma_y^2}{\mu_y^2} - \frac{\sigma_{xy}}{\mu_x \mu_y} \right). \end{aligned} \quad (5.7)$$

Similarly, variance of the rational is

$$\begin{aligned} \sigma_{x/y}^2 &= \left\langle \left(\frac{\mu_x + \Delta x}{\mu_y + \Delta y} \right)^2 \right\rangle - \mu_{x/y}^2 \\ &\simeq \frac{\mu_x^2}{\mu_y^2} \left(\frac{\sigma_x^2}{\mu_x^2} + \frac{\sigma_y^2}{\mu_y^2} - \frac{2\sigma_{xy}}{\mu_x \mu_y} \right). \end{aligned} \quad (5.8)$$

Now, ellipticity, ϵ , is defined as $\epsilon = 1 - \frac{p_3}{p_1} = 1 - \sqrt{\frac{I_3}{I_1}}$, where $p_1 \geq p_2 \geq p_3$ are the three principal axes of the ellipsoid, and $I_1 \geq I_2 \geq I_3$ are the eigenvalues of the inertia tensor I_{ij} . From $p_i^2 \propto I_i$, we have

$$\frac{\Delta p_i}{\mu_{p_i}} = \frac{1}{2} \frac{\Delta I_i}{\mu_{I_i}}, \quad (5.9)$$

and therefore, we have

$$\begin{aligned} \mu_\epsilon &= 1 - \mu_{p_3/p_1} \simeq 1 - \frac{\mu_{p_3}}{\mu_{p_1}} \left(1 + \frac{\sigma_{p_1}^2}{\mu_{p_1}^2} - \frac{\sigma_{p_1 p_3}}{\mu_{p_1} \mu_{p_3}} \right) \\ &= 1 - \sqrt{\frac{\mu_{I_3}}{\mu_{I_1}}} \left(1 + \frac{1}{4} \frac{\sigma_{I_1}^2}{\mu_{I_1}^2} - \frac{1}{4} \frac{\sigma_{I_1 I_3}}{\mu_{I_1} \mu_{I_3}} \right), \end{aligned} \quad (5.10)$$

and

$$\begin{aligned} \sigma_\epsilon^2 &= \sigma_{p_3/p_1}^2 \simeq \frac{\mu_{p_3}^2}{\mu_{p_1}^2} \left(\frac{\sigma_{p_1}^2}{\mu_{p_1}^2} + \frac{\sigma_{p_3}^2}{\mu_{p_3}^2} - \frac{2\sigma_{p_1 p_3}}{\mu_{p_1} \mu_{p_3}} \right) \\ &= \frac{1}{4} \frac{\mu_{I_3}^2}{\mu_{I_1}^2} \left(\frac{\sigma_{I_1}^2}{\mu_{I_1}^2} + \frac{\sigma_{I_3}^2}{\mu_{I_3}^2} - \frac{2\sigma_{I_1 I_3}}{\mu_{I_1} \mu_{I_3}} \right). \end{aligned} \quad (5.11)$$

From eq. (2.1), we have

$$I_{ij} \equiv \frac{1}{N_{\text{vg}}} \sum_{\alpha=1}^{N_{\text{vg}}} x_{i,\alpha} x_{j,\alpha}, \quad (5.12)$$

and in the continuous density field, we have

$$\begin{aligned} I_{ij} &\equiv \int_{V_{\text{void}}} d^3x \, n(\mathbf{x}) x_i x_j \\ &= \int_{V_{\text{void}}} d^3x \, [\bar{n} + \delta n(\mathbf{x})] x_i x_j = \mu_{I_{ij}} + \Delta I_{ij}, \end{aligned} \quad (5.13)$$

where

$$\mu_{I_{ij}} = \int_{V_{\text{void}}} d^3x \, \bar{n} x_i x_j, \quad (5.14)$$

$$\Delta I_{ij} = \int_{V_{\text{void}}} d^3x \, \delta n(\mathbf{x}) x_i x_j. \quad (5.15)$$

Also, the variance of the inertia tensor is given as

$$\sigma_{I_{ij}}^2 = \langle (\Delta I_{ij})^2 \rangle = \langle I_{ij}^2 \rangle - \mu_{I_{ij}}^2. \quad (5.16)$$

5.1 Void With a Well-defined Boundary: $\langle p_i \rangle \rightarrow P_i$

Let us calculate the bias in the mean and the variance of the ellipticity calculated from a rectangular void with a diagonalized inertia tensor of $I_1 \equiv I_{11}$, $I_2 \equiv I_{22}$ and $I_3 \equiv I_{33}$. The number of void galaxies is N_{vg} . Here, we assume an idealized setup, where the boundary shape of a void is well defined (i.e., $\langle p_i \rangle \rightarrow P_i$) to see whether the estimator of an output ellipticity based on the inertia tensor yields unbiased result. For more realistic estimate on the bias in mean and the variance of output ellipticities, see § 5.2.

For a rectangular void with volume, $V_{\text{void}} = 8P_1P_2P_3$ (i.e., $x_i \in [-P_i, P_i] \forall i$), where P_i is a well-defined length of the principal axis of the rectangular void, we have

$$\mu_{I_i} = \int_{V_{\text{void}}} d^3x \, \bar{n} x_i^2 = \frac{1}{3} \bar{n} V_{\text{void}} P_i^2 = \frac{1}{3} N_{\text{vg}} P_i^2, \quad (5.17)$$

and

$$\begin{aligned} \sigma_{I_i}^2 &= \int_{V_{\text{void}}} \int_{V'_{\text{void}}} d^3x d^3x' \, \langle n(\mathbf{x}) n(\mathbf{x}') \rangle x_i^2 x_i'^2 - \mu_{I_i}^2 \\ &= \int_{V_{\text{void}}} \int_{V'_{\text{void}}} d^3x d^3x' \, \bar{n} \delta_D(\mathbf{x} - \mathbf{x}') x_i^2 x_i'^2 - \mu_{I_i}^2 \\ &= \bar{n} \int_{V_{\text{void}}} d^3x \, x_i^4 - \mu_{I_i}^2 = \frac{1}{5} \bar{n} V_{\text{void}} P_i^4 - \mu_{I_i}^2 \\ &= \frac{1}{5} N_{\text{vg}} P_i^4 - \frac{1}{9} N_{\text{vg}}^2 P_i^4, \end{aligned} \quad (5.18)$$

where we have assumed that the distribution of void galaxies follows the Poisson statistics with $\langle n(\mathbf{x}) \rangle = \bar{n}$ and $\langle n(\mathbf{x}) n(\mathbf{x}') \rangle = \bar{n} \delta_D(\mathbf{x} - \mathbf{x}')$. Similarly, we have

$$\begin{aligned} \sigma_{I_i I_j} &= \bar{n} \int_{V_{\text{void}}} d^3x \, x_i^2 x_j^2 - \mu_{I_i} \mu_{I_j} \\ &= \frac{1}{9} N_{\text{vg}} P_i^2 P_j^2 - \frac{1}{9} N_{\text{vg}}^2 P_i^2 P_j^2, \end{aligned} \quad (5.19)$$

Therefore, Eqs(5.10) and (5.11) are re-written as follows,

$$\mu_\epsilon = 1 - \frac{P_3}{P_1} - \frac{P_3}{P_1} \frac{1}{5N_{\text{vg}}}, \quad (5.20)$$

$$\sigma_\epsilon^2 = \frac{P_3^2}{P_1^2} \frac{2}{5N_{\text{vg}}}. \quad (5.21)$$

We see that for a given rectangular void with $N_{\text{void}} = 20$, we can accurately extract its ellipticity from void galaxies to $\sim 1\%$, but its standard deviation remains significant (i.e., $\sigma_\epsilon \sim 0.14$ for a void with zero ellipticity). As is expected, the variance of ellipticity, σ_ϵ^2 , scales as inversely proportional to the number of void galaxies, N_{vg} . Note that the above result is derived in the limit of $\langle p_i \rangle \rightarrow P_i$.

5.2 Void With an Undefined Boundary: $\langle p_i \rangle \neq P_i$

With a small number of field galaxies randomly distributed inside the well-defined boundary, P_i , we generally have $\langle p_i \rangle \neq P_i$. For example, let us imagine a spherical boundary, where $P_1 = P_2 = P_3$ and $\epsilon_{\text{in}} = 1 - \frac{P_3}{P_1} = 0$, with $N_{\text{vg}} = 4$ field galaxies. This spherical boundary represents the shape of the underlying tidal field, and we sample this by 4 galaxies. No matter how we distribute those four galaxies, unless the four galaxies align at each of four apexes of an equilateral tetrahedron, calibrated ellipticity cannot be zero, $\epsilon_{\text{out}} \neq \epsilon_{\text{in}}$. As a result, we have a significant deviation of $\langle \epsilon_{\text{out}} \rangle$ from its boundary ellipticity, $\epsilon_{\text{in}} \equiv 1 - \frac{P_3}{P_1}$, and a correspondingly large standard deviation.

As we increase N_{vg} , those randomly scattered particles fill in the bounded space more densely, and $\langle \epsilon_{\text{out}} \rangle$ gradually approaches the boundary ellipticity, ϵ_{in} . This uncertainty in ϵ_{out} due to small N_{vg} introduces an additional bias and scatter to the ones given by eqs. (5.20) and (5.21).

For the case of elliptical voids, the analytic prediction of the mean and variance is non-trivial; thus, we have performed numerical experiments. First, we create an ellipsoidal boundary with a fixed size and ellipticity (i.e., P_1 , P_2 and P_3), and then fill this bounded volume by N_{vg} random particles. For each realization, we calculate the inertia tensor and its eigenvalues (p_1 , p_2 and p_3), where the output ellipticity is defined as

$$\epsilon_{\text{out}} \equiv 1 - \frac{p_3}{p_1}, \quad (5.22)$$

$$\eta_{\text{out}} \equiv 1 - \frac{p_2}{p_1}, \quad (5.23)$$

while the input ellipticity is defined as

$$\epsilon_{\text{in}} \equiv 1 - \frac{P_3}{P_1}, \quad (5.24)$$

$$\eta_{\text{in}} \equiv 1 - \frac{P_2}{P_1}. \quad (5.25)$$

Finally, we have a bias in the mean and variance of the output ellipticity, ϵ^{out} as follows

$$\langle \epsilon_{\text{out}} \rangle - \epsilon_{\text{in}} = \frac{P_3}{P_1} - \left\langle \frac{p_3}{p_1} \right\rangle, \quad (5.26)$$

$$\sigma_{\epsilon_{\text{out}}}^2 = \langle \epsilon_{\text{out}}^2 \rangle - \langle \epsilon_{\text{out}} \rangle^2. \quad (5.27)$$

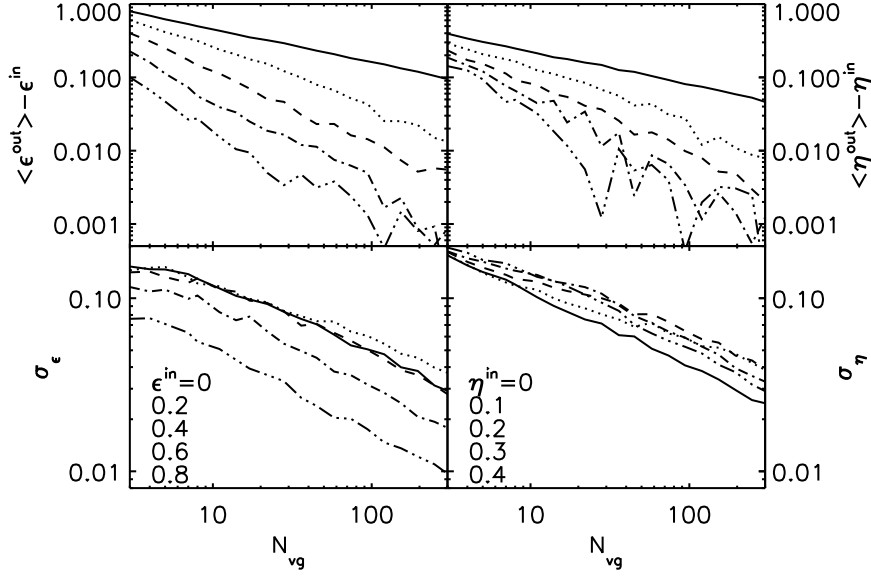


Figure 10. Bias and variance in the measured ellipticities. We place N_{vg} particles within a boundary of a given set of size and input ellipticities, ϵ^{in} and η^{in} , and calculate the mean ellipticities, $\langle \epsilon^{\text{out}} \rangle$ and $\langle \eta^{\text{out}} \rangle$, and their standard deviations σ_ϵ and σ_η , from 500 realizations for each N_{vg} and input ellipticity. Top figures show the biases in finding the input ellipticities (i.e., true underlying ellipticities of a tidal field), $\langle \epsilon^{\text{out}} \rangle - \epsilon^{\text{in}}$ and $\langle \eta^{\text{out}} \rangle - \eta^{\text{in}}$, and bottom figures show the standard deviations, σ_ϵ and σ_η .

Figure 10 shows the result of 500 realizations for a given set of ϵ^{in} and N_{vg} . The top figures show the bias in the mean of the ellipticities ϵ (left) and η (right), and the bottom figures show the standard deviations of ϵ (left) and η (right). We see that both bias in the mean and variance of ϵ_{out} are large enough to change the shape of ellipticity PDF significantly for $N_{\text{vg}} \lesssim 100$. In order to correct the ellipticity PDF, we define a response function, $R(\epsilon_{\text{out}}|\epsilon_{\text{in}}, N_{\text{vg}})$, such that

$$p(\epsilon_{\text{out}}|\sigma_{R_L}, \delta, N_{\text{vg}}) = \int d\epsilon_{\text{in}} R(\epsilon_{\text{out}}|\epsilon_{\text{in}}, N_{\text{vg}}) p(\epsilon_{\text{in}}|\sigma_{R_L}, \delta). \quad (5.28)$$

In figure 11, we show the normalized histograms for the number of voids with output ellipticity, ϵ_{out} , from the numerical simulation with a given N_{vg} and ϵ_{in} . We also show Gaussian distributions (red lines) with the mean $\langle \epsilon_{\text{out}} \rangle$ and variance $\sigma_{\epsilon_{\text{out}}}^2$,

$$R(\epsilon_{\text{out}}|\epsilon_{\text{in}}, N_{\text{vg}}) = \frac{1}{\sqrt{2\pi\sigma_{\epsilon_{\text{out}}}^2}} \exp \left[-\frac{(\epsilon_{\text{out}} - \langle \epsilon_{\text{out}} \rangle)^2}{2\sigma_{\epsilon_{\text{out}}}^2} \right], \quad (5.29)$$

where both mean and variance are functions of the input ellipticity and the number of void galaxies (i.e., $\langle \epsilon_{\text{out}} \rangle = \langle \epsilon_{\text{out}}(\epsilon_{\text{in}}, N_{\text{vg}}) \rangle$ and $\sigma_{\epsilon_{\text{out}}} = \sigma_{\epsilon_{\text{out}}}(\epsilon_{\text{in}}, N_{\text{vg}})$). In figure 12, we show the ellipticity PDF without the correction for the response function (black lines) as well as the corrected ellipticity PDF (red lines) for four different redshifts, $z = 0$ (solid), 1 (dotted), 2

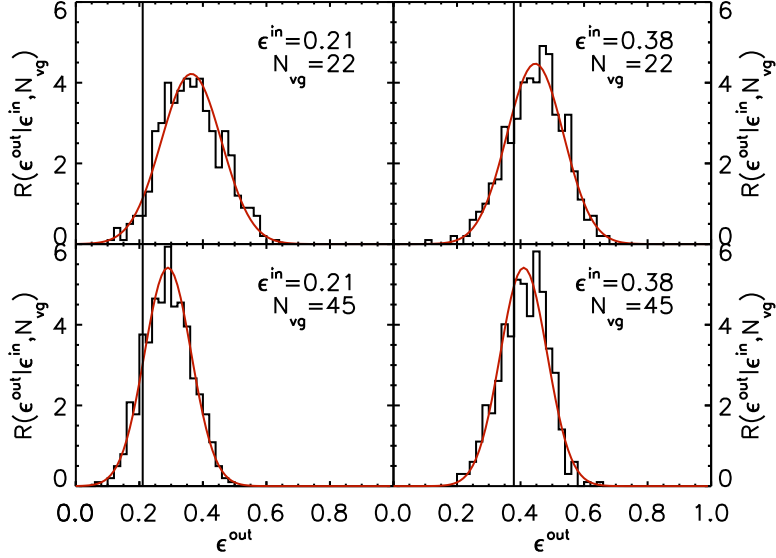


Figure 11. We show the normalized histograms of output ellipticities, ϵ_{out} for a fixed input ellipticity, ϵ_{in} , and a number of void galaxies, N_{vg} . We find that the Gaussian profile of eq. (5.29) with mean, $\langle \epsilon_{\text{out}} \rangle$, and variance, $\sigma_{\epsilon_{\text{out}}}$, fits the measured histograms (red lines) well. Also, we show the locations of the input ellipticity, ϵ_{in} , with vertical lines.

(dashed) and 3 (dot-dashed) with different values of N_{vg} . Here, we use $R_L = 4\text{Mpc}^{-1}$ and $\delta_m = -0.9$ to calculate the original PDFs at four different redshifts. We see that the shapes of PDF with higher redshifts are more susceptible to the small N_{vg} effect. For a typical void studied in PL07 using the Millennium Run catalog at $z = 0$, N_{vg} is roughly between 20 to 60, R_L ranges from 4 to $6.4h^{-1}\text{Mpc}$, and $\delta_v \sim -0.9$. We clearly see that voids with small initial ellipticity ϵ_{in} are most vulnerable to the Poisson noise, and with $N_{\text{vg}} \sim 10$, the original shape of ellipticity PDF is almost washed out to leave only the distribution of the Poisson noise. On the other hand, the ellipticity PDF at low redshift ($z = 0$) maintains its original shape with the number of void galaxies as small as $N_{\text{vg}} \lesssim 45$. In short, a shape with small ellipticity is hard to trace with a small number of tracers. For example, if we have a sphere of radius $R = 10h^{-1}\text{Mpc}$ in the simulation box with a resolution of $1h^{-1}\text{Mpc}$, the possible number of configurations of randomly scattered tracing particles with $N_{\text{vg}} = 4$ will be ${}_{4187}C_4 \sim 1.3 \times 10^{13}$, while the possible number of configurations of an equilateral tetrahedron (i.e., $\epsilon = 0$) is vanishingly small. Also, the scatter of the output ellipticity σ_ϵ will not center around ϵ_{in} for a small ellipticity as $0 \leq \epsilon \leq 1$, and as a result, $\langle \epsilon_{\text{out}} \rangle$ converges to ϵ_{in} only slowly as we increase N_{vg} . On the other hand, the ellipticity of a highly elongated shape can be well traced even with a limited number of tracers.

For $N_{\text{vg}} \lesssim 100$, we use a fitting function derived from figure 10,

$$\langle \epsilon_{\text{out}} \rangle - \epsilon_{\text{in}} = \alpha_1(\epsilon_{\text{in}}) N_{\text{vg}}^{-\beta_1(\epsilon_{\text{in}})} \quad (5.30)$$

$$\sigma_{\epsilon_{\text{out}}} = \alpha_2(\epsilon_{\text{in}}) N_{\text{vg}}^{-\beta_2(\epsilon_{\text{in}})}, \quad (5.31)$$

where α_1 , α_2 , β_1 , and β_2 are given as polynomials to the third order, $p_0 + p_1\epsilon_{\text{in}} + p_2\epsilon_{\text{in}}^2 + p_3\epsilon_{\text{in}}^3$, and we show the best-fit coefficients, p_0 , p_1 , p_2 and p_3 in table 1.

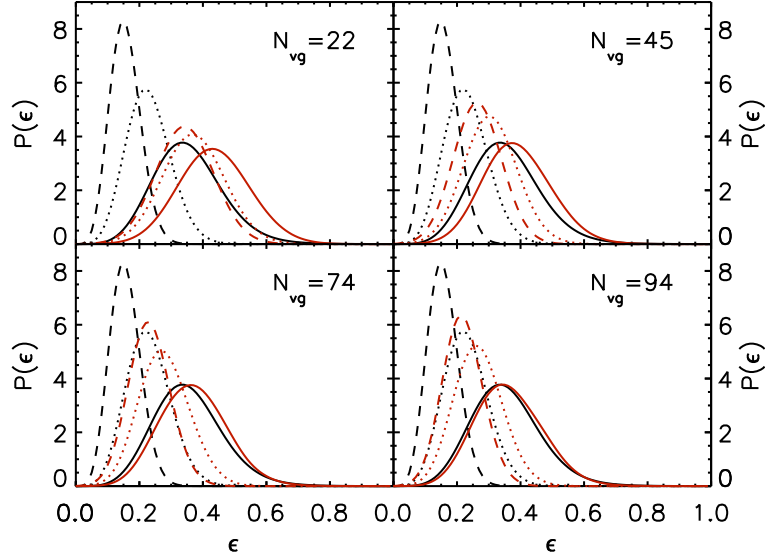


Figure 12. We show the real space ellipticity PDFs without Poisson noise (black lines) at $z = 0$ (solid), 1 (dotted) and 2 (dashed). We then convolve each noise-free PDF with the response function given by eq. (5.29), and show the resulting PDFs for four different N_{vg} (red lines).

	p_0	p_1	p_2	p_3
α_1	1.282	2.384	-7.280	3.587
α_2	0.2636	-0.3103	0.9557	-0.9404
β_1	0.4500	1.708	-0.8460	-0.02668
β_2	0.3650	-0.6260	1.680	-0.9296

Table 1. We show the best-fit coefficients, p_0 , p_1 , p_2 and p_3 for α_1 , α_2 , β_1 , and β_2 of eqs. (5.30) and (5.31), where α_1 , α_2 , β_1 , and β_2 are given as polynomials to the third order, $p_0 + p_1\epsilon_{\text{in}} + p_2\epsilon_{\text{in}}^2 + p_3\epsilon_{\text{in}}^3$.

6 Voids from N-body Simulation

To test the analytic predictions made in the previous sections, we use a catalog of galaxies from the Millennium simulation [5, 6]. In a comoving box of $L_{\text{box}} = 500 h^{-1}\text{Mpc}$, there are 26690265, 26359329, and 23885840 galaxies in the simulation at $z = 0$, 1, and 2, respectively. For each redshift, we select a subset of galaxies whose halo masses are above $M_h = 2.6 \times 10^{12}$, 2.6×10^{12} , and $8.6 \times 10^{11} h^{-1} M_{\odot}$. We find 182081, 121454, and 261471 such halos for $z = 0$, 1, and 2, respectively.

Here, we use the void finding algorithm of FN09 to identify voids from the subsets of galaxies. Their algorithm first divides a given set of galaxies into wall galaxies, which define boundaries of holes, and void galaxies, which are allowed to be within holes by calculating the distances to the third nearest galaxies, D_3 . When a galaxy has the third nearest distance, D_3 , smaller than the user-defined threshold distance, $R_3 > D_3$, the galaxy is labeled as a wall galaxy, and when $R_3 < D_3$, the galaxy is labeled as a void galaxy. Here, $R_3 \equiv \langle D_3 \rangle + \lambda \sigma_{D_3}$, where $\langle D_3 \rangle$ and σ_{D_3} are the mean third distance and its standard deviation, respectively,

and λ is a user-defined parameter. We use the value of $\lambda = 2$ recommended by FN09. Then, a hole is defined as a sphere with maximal radius in a galaxy distribution containing no wall galaxy, and by definition, a hole can contain void galaxies. Finally, a void is identified by the subsequent merger of neighboring holes with user-defined criteria (i.e., a percentage of volume overwraps with the neighboring holes and a minimum size of hole, ξ), where, we use $\xi = 1.5R_3$. As a result, voids identified by the algorithm of FN09 have aspherical shape with a finite number of void galaxies within. For each identified void, FN09 found a volume, a size and an ellipticity of the best-fit ellipsoid by calculating the inertia tensor from randomly scattered particles within the boundary of the void.

Using a void-finder of FN09, we identify 569, 327, and 804 voids for $z = 0, 1$, and 2 , respectively. Here, as we noted earlier, since we are interested in a shape of a tidal field near the density minima, we have modified the void finding algorithm of FN09 so that an ellipticity of a void can be evaluated from the distributions of galaxies inside a void (i.e., we directly calculate an inertia tensor from void galaxies, not from randomly scattered particles as in FN09).

With this modification, the extracted ellipticity PDF has a closer contact with the analytic ellipticity PDF derived from the tidal field of the local minima of the density field.

We measure the linear galaxy biases by comparing the galaxy power spectra of input galaxy distributions against linear matter power spectra from CAMB at each redshift. In figure 13, we show the linear matter power spectra, $P_m(k)$, from CAMB with the cosmological parameters same as the Millennium simulation (i.e., $\Omega_m = 0.25$, $\Omega_\Lambda = 0.75$, $n_s = 1$ and $\sigma_8 = 0.9$) (solid), linear galaxy spectra, $P_g(k) = b_L^2 P_m(k)$, (dotted) and power spectra of the subset of galaxies from the Millennium simulation (crosses with error bars) at $z = 0$ (top), 1 (middle) and 2 (bottom). With fittings up to $k_{max} = 0.03h \text{ Mpc}^{-1}$ (i.e., using the first two data points of $P_g(k)$), we find $b_L = 1.0, 1.6$, and 2.0 for $z = 0, 1$, and 2 , respectively. Here, non-linearity of the power spectrum is rather small at this scale, $k < 0.03h \text{ Mpc}^{-1}$.

In figure 14, we show the ellipticity PDF extracted from the Millennium simulation at $z = 0$ (top), 1 (middle) and 2 (bottom) together with the analytic ellipticity PDF corrected for the linear galaxy biases and response functions (red lines). As references, we also show the analytic ellipticity PDF (black lines) with (dotted black lines) and without the linear galaxy bias (solid black lines). We also show the $1\text{-}\sigma$ range of the histograms calculated with bootstrapping method (grey).

Here, for each redshift, we demand voids have at least 10 void galaxies. Table 2 shows redshifts, z , the numbers of voids used to draw histograms, N_v , the minimum numbers of void galaxies per void, $N_{vg,min}$, the median numbers of void galaxies per void, $N_{vg,med}$, the linear galaxy biases, b_L , the mean density contrasts of void, $\bar{\delta}_v$, the mean Eulerian radii of voids, $\bar{R}_E \equiv (\bar{p}_1 \bar{p}_2 \bar{p}_3)^{1/3}$, the mean ellipticities of extracted voids, $\bar{\epsilon}^{obs}$, and those of the analytic PDF, $\bar{\epsilon}^{theory}$, and the errors in the mean, $\Delta\epsilon^{obs}$.

We find from the figure 14 that the analytic ellipticity PDFs convolved with the response function (red lines) show a good agreement with the extracted ellipticity PDFs from the simulations, with the chi square values of $\chi^2 = 23.0, 16.9$ and 20.1 with the degrees of freedom of 15, 16 and 13 for redshifts of $z = 0, 1.078$ and 2.070 , respectively. We test the null hypothesis that the extracted ellipticity PDF is drawn from the analytic ellipticity PDF convolved with the response function, calculating the probability-to-exceed (PTE) the measured χ^2 ,

$$\alpha = \int_{\chi^2}^{\infty} P_n(x) dx, \quad (6.1)$$

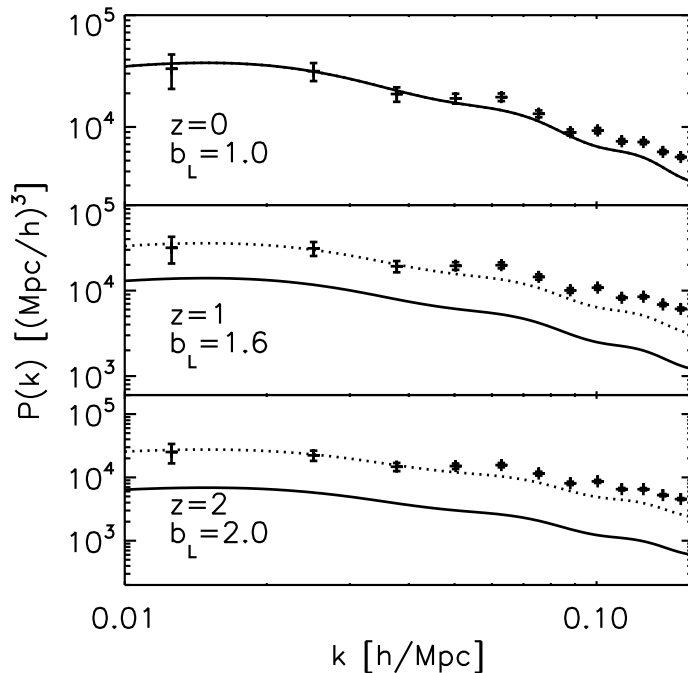


Figure 13. We show the linear matter power spectra, $P_m(k)$, from CAMB with the cosmological parameters same as the Millennium simulation (i.e., $\Omega_m = 0.25$, $\Omega_\Lambda = 0.75$, $n_s = 1$ and $\sigma_8 = 0.9$) (solid), linear galaxy spectra, $P_g(k) = b_L^2 P_m(k)$, (dotted) and power spectra of the subset of galaxies from the Millennium simulation (crosses with error bars) at $z = 0$ (top), 1 (middle) and 2 (bottom).

where $P_n(x)$ is a PDF of χ^2 -distribution with a n -degree of freedom,

$$P_n(x) = \frac{x^{n/2-1} e^{-x/2}}{2^{n/2} \Gamma(n/2)}. \quad (6.2)$$

We find that our analytic model is consistent with the void ellipticity PDF extracted from the Millennium simulation with PTE = 0.12, 0.39 and 0.094 for redshifts of $z = 0$, 1.078 and 2.070, respectively.

Although we have good fits for all redshifts, the extracted ellipticity PDFs are entirely dominated by the Poisson noise due to the small number of void galaxies, $N_{\text{vg}} \ll 100$. To see this, we have performed a null test with a top-hat PDF with the mean and the width equal to the analytic ellipticity PDF. After convolving the top-hat PDF with the response functions, we find an equally good fit with a similar χ^2 . We repeat the null tests for different values of the mean and the width of the analytic ellipticity PDF. We find that the extracted ellipticity PDF is well fitted with an arbitrary shape of PDF, whose mean ellipticity is the same as the one predicted from the analytic ellipticity PDF, convolved with the response function.

6.1 Comments on the Void-Finder Dependence

In this work, we have assumed that voids are the local minima of density field with three dimensionally expanding volume. In the Lagrangian picture, this is equivalent to having all

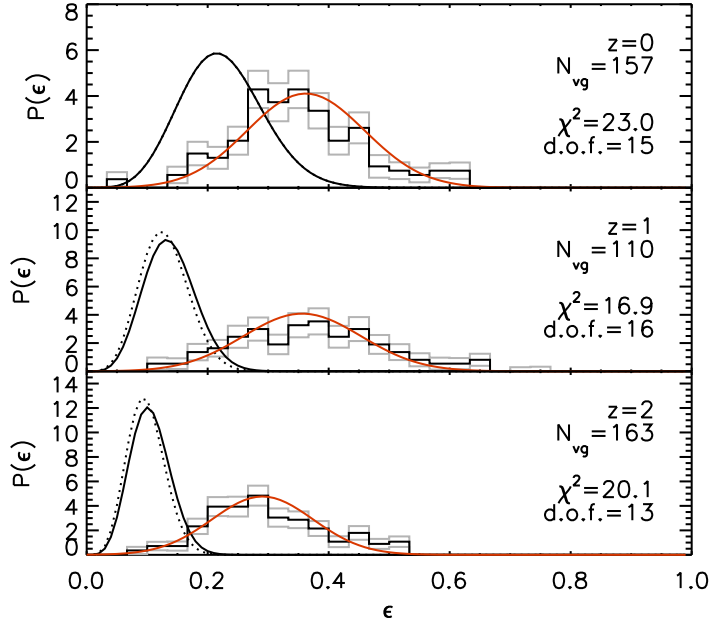


Figure 14. We show the ellipticity PDF extracted from the Millennium simulation at $z = 0$ (top), 1 (middle) and 2 (bottom) together with the analytic ellipticity PDF corrected for galaxy biases and convolved with the response functions (red lines). As references, we also show the analytic ellipticity PDF (black lines) with (dotted black lines) and without galaxy bias (solid black lines). We also show the $1 - \sigma$ range of the histogram, σ_ϵ , estimated via the bootstrap method (gray histograms). For each redshift, the chi-square values are $\chi^2 = 21.5$, 17.0 and 20.0 , and the degree of freedoms are 15 , 16 and 13 for $z = 0$, 1 and 2 , respectively.

z	N_v	$N_{\text{vg,min}}$	$N_{\text{vg,med}}$	b_L	δ_v	\bar{R}_E	$\bar{\epsilon}^{\text{obs}}$	$\bar{\epsilon}^{\text{theory}}$	$\Delta\epsilon^{\text{obs}}$
0	157	15	19	1.0	-0.66	21.8	0.343	0.360	0.008
1.078	110	10	15	1.6	-0.59	21.9	0.377	0.356	0.012
2.070	163	20	24	2.0	-0.60	19.9	0.302	0.291	0.008

Table 2. We show the statistics of voids used to make the histogram in the figure 14. From left to right, we have redshifts, z , numbers of voids used to draw histograms, N_v , minimum numbers of void galaxies per void, $N_{\text{vg,min}}$, median numbers of void galaxies per void, $N_{\text{vg,med}}$, linear galaxy biases, b_L , mean density contrasts of void, δ_v , mean Eulerian radii of voids, $\bar{R}_E \equiv (\overline{p_1 p_2 p_3})^{1/3}$ ($h^{-1}\text{Mpc}$), mean ellipticities of extracted voids, $\bar{\epsilon}^{\text{obs}}$, and those of analytic PDF, $\bar{\epsilon}^{\text{theory}}$, and errors in the mean, $\Delta\epsilon^{\text{obs}}$.

the eigenvalues of the tidal tensor, $T_{ij} \equiv \partial_i \partial_j \Psi(\mathbf{q})$, being negative (i.e., $\lambda_3 \geq \lambda_2 \geq \lambda_1 < 0$, and $\sum_{i=1}^3 \lambda_i = \delta_m$).

However, as Lavaux & Wandelt [19] pointed out, in a saddle-like density distribution, voids can contract along one of the axis, while it expands along the rest of the axes. Lavaux & Wandelt [19] studied these spurious voids in the Lagrangian picture together with their own void-finding algorithm (DIVA). They found that among those spurious voids, pancake voids (i.e., two dimensionally expanding, one dimensionally contracting voids) are as abundant as three dimensionally expanding genuine voids, and the shape of the ellipticity distribution

function of PL07 needs to be modified. Nevertheless, we focused our work on the three dimensionally expanding voids, as the result of PL07 suggests that the void finding algorithm of Hoyle & Vogeley [12] mostly finds three dimensionally expanding genuine voids. There seems to be an algorithm dependent selection of the type of voids.

FN09 reported a slight preference for prolate ellipsoids in the ellipticity PDF drawn from voids detected in the SDSS DR5, while the analytic ellipticity PDF of PL07 shows a clear preference for oblate ellipsoids. FN09 used the best-fit ellipsoid of Jang-Condell & Hernquist [15] to estimate the ellipticity of a void with a Monte-Carlo simulation. For each realization, they calculated an inertia tensor for each void from test particles randomly spread inside the void. In this way, their measurements of ellipticity tend to be more sensitive to the shape of the void boundary (i.e., $I_{ij} \propto p_i p_j$). On the other hand, PL07 uses field galaxies *inside* the void to calculate the inertia tensor. An ellipticity calculated from void galaxies is more sensitive to the shape of the tidal field around a density minimum, and therefore, has a closer contact with the analytic ellipticity PDF of PL07. Indeed, the mean effective volume of voids, $V_{\text{eff}} = \frac{4\pi}{3} p_1 p_2 p_3$, extracted from the Millennium simulation with the method of PL07 is ~ 4 times smaller than that of FN09 (i.e., most void galaxies are within $\sim 60\%$ of radius from the void center).

7 Discussion and Conclusion

We have derived the ellipticity PDF of voids in the redshift space. We have found that the redshift space distortion on the shape of voids statistically increases the ellipticities of voids, and leaves a prominent feature on the ellipticity PDF as a substantial reduction in the probability of having voids with small ellipticity, $\epsilon < -\frac{f\delta}{3}$. This characteristic cutoff in the ellipticity PDF can be used as a probe of the growth rate, $f(a) \equiv \frac{d \ln D_+(a)}{d \ln a}$, once the radial density profile of voids is better understood. Acquaviva & Gawiser [1] proposed a model independent test of GR by checking the scale dependence/independence of the growth rate, $f(k, z)$ from a galaxy power spectrum at small scale, $P_g(k_S, z)$, and large scale $P_g(k_L, z)$. In principle, we can use the redshift space ellipticity PDF of a void to measure the growth rate at different scales by binning the observed voids into small and large sizes.

However, as we have shown in § 5, the biggest limiting factor for the use of ellipticity PDF as a probe of cosmology lies in the Poisson noise from a small number of N_{vg} inside a given void. We have found that from a sample of galaxies with a minimum halo mass of $2.6 \times 10^{12} h^{-1} M_\odot$ for $z = 0$ and 1, and $8.6 \times 10^{11} h^{-1} M_\odot$ for 2, we have $N_{\text{vg}} \sim 20$ void galaxies per each identified void. This small number of void galaxies per each void creates a significant contamination of the resulting ellipticity PDF so that the shape of the original PDF is almost washed-out.

As we have seen, the biggest limiting factor for the use of ellipticity PDF as a probe of cosmology lies in the Poisson noise from a small number of N_{vg} inside a given void. We have found that from a sample of galaxies with a minimum halo mass of $2.6 \times 10^{12} h^{-1} M_\odot$ for $z = 0$ and 1, and $8.6 \times 10^{11} h^{-1} M_\odot$ for 2, we have $N_{\text{vg}} \sim 20$ void galaxies per each identified void. This small number of void galaxies per each void creates a significant contamination of the resulting ellipticity PDF so that the shape of the original PDF is almost washed-out.

Nevertheless, there is a way to overcome the Poisson noise. Recently, Lavaux & Wandelt [20] proposed the stacking analysis of the void ellipticity in the redshift space as a way to put a constraint on the cosmological parameters via the Alcock Paczynski (AP) test [2]. The AP test uses the deviation from the isotropy and homogeneity of the observed structure, which

is known to be spherical (e.g., galaxy distributions at large scale), to determine $D_A H$. For example, when one calibrates comoving distances perpendicular, r_\perp , and parallel to the line of sight, r_\parallel , from the angular, θ , and redshift, z , distribution of galaxies with

$$\theta = \frac{r_\perp(z)}{(1+z)D_A(z)}, \quad (7.1)$$

$$\delta z = \frac{r_\parallel(z)H(z)}{c}, \quad (7.2)$$

one need to assume a reference cosmological model to calculate $D_A^{\text{ref}}(z)$ and $H^{\text{ref}}(z)$. If the observed structure has $r_\perp = r_\parallel$, and we have observed values of the angular, θ , and the redshift, z , distributions of galaxies, a combination of D_A and H can be constrained as follows,

$$D_A(z)H(z) = \frac{c\delta z}{(1+z)\theta} \quad (7.3)$$

(see, e.g., Kazin et al. [17], Shoji et al. [37] for the use of AP test on the two-dimensional power spectrum, $P(k, \mu)$).

In real space, the stacked void with sufficient number of stacked void galaxies should have zero ellipticity, while the deviation from zero ellipticity in real space indicates the deviation of the assumed cosmology from the true cosmology. In redshift space, since the void is elongated toward the line of sight, the stacked void has non-zero ellipticity, which can be a tell-tale of the logarithmic growth rate, $f(a) = \frac{d \ln D_+(a)}{d \ln a}$. Although some useful information of void ellipticity will be lost by stacking, in this way, we can see the effect of redshift space distortion as a source of anisotropy in the stacked void ellipticity. We think that the stacking analysis of the voids in redshift space is potentially a powerful tool to probe the cosmology.

Acknowledgments

MS would like to thank Caroline Foster for letting us use their void-finder, which was used in § 6 of this paper. MS would also thank M. Kubota and E. Komatsu for their warm hospitality and affectionate supervision. The Millennium Simulation databases used in this paper and the web application providing on-line access to them were constructed as part of the activities of the German Astrophysical Virtual Observatory.

A Calculation of $\kappa(\mathbf{x})$

A mapping between the real-space to the redshift space is

$$x_1^s = x_1^r \quad (A.1)$$

$$x_2^s = x_2^r \quad (A.2)$$

$$x_3^s = x_3^r - f \mathbf{u} \cdot \hat{\mathbf{x}}_3^r, \quad (A.3)$$

where $f \equiv \frac{d \ln \delta(a)}{d \ln a}$ is the growth rate, and we set the unit vector, $\hat{\mathbf{x}}_3^r$, to be along the line of sight direction. Here, $\mathbf{u} \equiv \frac{-\mathbf{v}}{\mathcal{H}f}$, where \mathbf{v} is the peculiar velocity of a void galaxy, and $\mathcal{H}(z)$ is a comoving Hubble rate.

We define $\kappa(\mathbf{x}^r)$ to quantify the strength of the redshift space distortion as follows

$$\kappa(\mathbf{x}^r) \equiv -\frac{f\hat{\mathbf{x}}_3^r \cdot \mathbf{u}(\mathbf{x}^r)}{x_3^r}, \quad (\text{A.4})$$

and we re-write eq. (A.3) as

$$x_3^s = x_3^r(1 + \kappa(\mathbf{x}^r)). \quad (\text{A.5})$$

Here, we use a spherical coordinate such that

$$x_1 = x \sin \theta_x \cos \phi_x \quad (\text{A.6})$$

$$x_2 = x \sin \theta_x \sin \phi_x \quad (\text{A.7})$$

$$x_3 = x \cos \theta_x \quad (\text{A.8})$$

and

$$k_1 = k \sin \theta_k \cos \phi_k \quad (\text{A.9})$$

$$k_2 = k \sin \theta_k \sin \phi_k \quad (\text{A.10})$$

$$k_3 = k \cos \theta_k, \quad (\text{A.11})$$

where $x \equiv |\mathbf{x}| = \sqrt{x_1^2 + x_2^2 + x_3^2}$, $k \equiv |\mathbf{k}| = \sqrt{k_1^2 + k_2^2 + k_3^2}$, and θ and ϕ are the azimuthal and inclination angles respectively.

$$\begin{aligned} \kappa(\mathbf{x}^r) &\equiv -\frac{f\hat{\mathbf{x}}_3^r \cdot \mathbf{u}(\mathbf{x}^r)}{x_3^r} = -\frac{f\hat{\mathbf{x}}_3^r \cdot \nabla \Phi(\mathbf{x}^r)}{4\pi G a^2 \bar{\rho} x_3^r} \\ &= -\frac{f}{4\pi G a^2 \bar{\rho} x_3^r} \int \frac{d^3 k}{(2\pi)^3} i\mathbf{k} \cdot \hat{\mathbf{x}}_3^r \tilde{\Phi}(\mathbf{k}) e^{i\mathbf{k} \cdot \mathbf{x}^r} \\ &= \frac{f}{x_3^r} \int \frac{d^3 k}{(2\pi)^3} i\mathbf{k} \cdot \hat{\mathbf{x}}_3^r \frac{\tilde{\delta}(\mathbf{k})}{k^2} e^{i\mathbf{k} \cdot \mathbf{x}^r} \\ &= \frac{f}{x_3^r} \int_0^\infty \frac{dk}{(2\pi)^3} i k \int_0^{2\pi} d\phi_k \int_{-1}^1 d\mu_k \mu_k \tilde{\delta}(\mathbf{k}) e^{i\mathbf{k} \cdot \mathbf{x}^r}, \end{aligned} \quad (\text{A.12})$$

where $\mu_k \equiv \cos \theta_k$. Here, $\mathbf{k} \cdot \mathbf{x} = kx \cos \gamma$, where

$$\cos \gamma \equiv \cos \theta_k \cos \theta_x + \cos(\phi_k - \phi_x) \sin \theta_k \sin \theta_x. \quad (\text{A.13})$$

A.1 Spherical Void

As for the spherical void of radius R with homogeneous top-hat density contrast, $\delta(\mathbf{x})$, we have

$$\tilde{\delta}(\mathbf{k}) = \bar{\delta} \int d^3 x' e^{-i\mathbf{k} \cdot \mathbf{x}'} = 4\pi \bar{\delta} \int_0^R dx x^2 e^{-ikx} = 4\pi R^3 \bar{\delta} \frac{j_1(kR)}{kR}. \quad (\text{A.14})$$

Therefore, eq. (A.12) becomes

$$\kappa(\mathbf{x}^r) = \frac{4\pi R^3 f \bar{\delta}}{x_3^r} \int_0^\infty \frac{dk}{(2\pi)^3} i k \frac{j_1(kR)}{kR} \int_0^{2\pi} d\phi \int_{-1}^1 d\mu_k \mu_k e^{i\mathbf{k} \cdot \mathbf{x}^r}. \quad (\text{A.15})$$

We first integrate the angular portion of the integration, $\int d\Omega_k \mu_k e^{i\mathbf{k} \cdot \mathbf{x}^r}$, expanding the exponent into Legendre polynomials,

$$e^{i\mathbf{k} \cdot \mathbf{x}^r} = \sum_l^{\infty} (-i)^l (2l+1) j_l(-kx) P_l(\cos \gamma), \quad (\text{A.16})$$

and using the Spherical harmonics addition theorem (a.k.a., Legendre addition theorem),

$$\begin{aligned} P_l(\cos \gamma) &= \frac{4\pi}{2l+1} \sum_{m=-l}^l (-1)^m Y_l^m(\theta_k, \phi_k) Y_l^{-m}(\theta_x, \phi_x) \\ &= \frac{4\pi}{2l+1} \sum_{m=-l}^l Y_l^m(\theta_k, \phi_k) \bar{Y}_l^m(\theta_x, \phi_x) \\ &= P_l(\cos \theta_k) P_l(\cos \theta_x) \\ &\quad + 2 \sum_{m=1}^l \frac{(l-m)!}{(l+m)!} P_l^m(\cos \theta_k) P_l^m(\cos \theta_x) \cos[m(\phi_k - \phi_x)], \end{aligned} \quad (\text{A.17})$$

where $P_l^m(x)$ is an associated Legendre polynomial, and it is related to the unassociated Legendre polynomial such that

$$\begin{aligned} P_l^m(x) &= (-1)^m (1-x^2)^{m/2} \frac{d^m}{dx^m} P_l(x) \\ &= \frac{(-1)^m}{2^l l!} (1-x^2)^{m/2} \frac{d^{l+m}}{dx^{l+m}} (x^2-1)^l. \end{aligned} \quad (\text{A.18})$$

Therefore,

$$\begin{aligned} \int d\Omega_k \mu_k e^{i\mathbf{k} \cdot \mathbf{x}^r} &= \sum_l^{\infty} (-i)^l (2l+1) j_l(-kx) \int d\Omega_k \mu_k P_l(\cos \gamma) \\ &= \sum_l^{\infty} \sum_{m=-l}^l (-i)^l (2l+1) j_l(-kx) \left(\frac{4\pi}{2l+1} \right)^{3/2} \\ &\quad \times Y_l^{-m}(\theta_x, \phi_x) \int d\Omega_k Y_1^0(\theta_k, \phi_k) \bar{Y}_l^{-m}(\theta_k, \phi_k) \\ &= \sum_l^{\infty} \sum_{m=-l}^l (-i)^l (2l+1) j_l(-kx) \left(\frac{4\pi}{2l+1} \right)^{3/2} Y_l^{-m}(\theta_x, \phi_x) \delta_{m0} \delta_{l1} \\ &= -3i j_1(-kx) \left(\frac{4\pi}{3} \right)^{3/2} Y_1^0(\theta_x, \phi_x) = 4\pi i j_1(kx) \cos \theta_x, \end{aligned} \quad (\text{A.19})$$

where we used $Y_1^0(\theta, \phi) = \sqrt{\frac{3}{4\pi}} \cos \theta$ and $j_l(-x) = (-1)^l j_l(x)$.

Finally, we obtain κ for a spherical void as

$$\begin{aligned}
\kappa(\mathbf{x}^r) &= \frac{4\pi R^3 f \bar{\delta}}{x_3^r} \int_0^\infty \frac{dk}{(2\pi)^3} i k \frac{j_1(kR)}{kR} [4\pi i j_1(kx) \cos \theta_x] \\
&= -\frac{2R^2 f \bar{\delta} \cos \theta_x}{\pi x_3^r} \int_0^\infty dk j_1(kR) j_1(kx) \\
&= -\frac{2R^2 f \bar{\delta} \cos \theta_x}{\pi x_3^r} \left(\frac{\pi x}{6R^2} \right) = -\frac{f \bar{\delta}}{3}.
\end{aligned} \tag{A.20}$$

A.2 Spheroidal Void with azimuthal symmetry

Here, we consider a spheroidal void with an azimuthal symmetry (i.e., an ellipsoid with two of the three principal axes have the same length, $a = b \neq c$). We again choose a spherical coordinate, but with the ellipsoidal volume element being projected on to spherical volume element such that

$$x_1 = a r \sin \theta \cos \phi \tag{A.21}$$

$$x_2 = a r \sin \theta \sin \phi \tag{A.22}$$

$$x_3 = c r \cos \theta, \tag{A.23}$$

where $0 \leq r \leq 1$ and $d^3x = a^2 c r^2 dr d\phi d\cos \theta$.

First, let us derive the Fourier transform of the spheroidal void with a homogeneous top-hat density contrast, $\delta(\mathbf{x})$ as follows,

$$\tilde{\delta}(\mathbf{k}) = \bar{\delta} \int d^3x e^{-i\mathbf{k} \cdot \mathbf{x}} = a^2 c \bar{\delta} \int_0^1 r^2 dr \int d\Omega e^{-i\mathbf{k} \cdot \mathbf{x}}, \tag{A.24}$$

where

$$\mathbf{k} \cdot \mathbf{x} = kr[a \sin \theta_k \sin \theta_x \cos(\phi_k - \phi_x) + c \cos \theta_k \cos \theta_x]. \tag{A.25}$$

Here, we define

$$\cos \gamma_a \equiv \sin \theta_k \sin \theta_x \cos(\phi_k - \phi_x) \tag{A.26}$$

$$\cos \gamma_c \equiv \cos \theta_k \cos \theta_x, \tag{A.27}$$

and

$$\cos \gamma \equiv \cos \gamma_a + \cos \gamma_c \tag{A.28}$$

$$\cos \eta \equiv -\cos \gamma_a + \cos \gamma_c, \tag{A.29}$$

where $\cos \eta$ is obtained by changing a sign of θ_x . In terms of $\cos \gamma$ and $\cos \eta$, we have

$$\mathbf{k} \cdot \mathbf{x} = \frac{1}{2} kr[(c + a) \cos \gamma + (c - a) \cos \eta]. \tag{A.30}$$

Again, we use the spherical harmonics addition theorem (eq. (A.17)). Note that due to the definition of eq. (A.29) and from eq. (A.17), we see that $P_l(\cos \eta) = P_l(\cos \gamma)$, and therefore,

$$\begin{aligned}
e^{-i\mathbf{k}\cdot\mathbf{x}} &= \exp\left[-\frac{1}{2}ikr(c+a)\cos\gamma\right]\exp\left[-\frac{1}{2}ikr(c-a)\cos\eta\right] \\
&= \left[\sum_{l=0}^{\infty}(-i)^l(2l+1)j_l\left(\frac{1}{2}kr(c+a)\right)P_l(\cos\gamma)\right] \\
&\quad \times \left[\sum_{l'=0}^{\infty}(-i)^{l'}(2l'+1)j_{l'}\left(\frac{1}{2}kr(c-a)\right)P_{l'}(\cos\gamma)\right] \\
&= \sum_{l=0}^{\infty}\sum_{l'=0}^{\infty}(-i)^{l+l'}(2l+1)(2l'+1)j_l\left(\frac{1}{2}kr(c+a)\right) \\
&\quad \times j_{l'}\left(\frac{1}{2}kr(c-a)\right)P_l(\cos\gamma)P_{l'}(\cos\gamma).
\end{aligned} \tag{A.31}$$

From the Legendre addition theorem, we have

$$\begin{aligned}
&\int d\Omega_x P_l(\cos\gamma)P_{l'}(\cos\gamma) \\
&= \frac{(4\pi)^2}{(2l+1)(2l'+1)}\sum_{m=-l}^l\sum_{m'=-l'}^{l'}(-1)^m Y_l^m(\theta_k, \phi_k)Y_{l'}^{m'}(\theta_k, \phi_k) \\
&\quad \times \int_0^{2\pi} d\phi_x \int_{-1}^1 d\cos\theta_x Y_l^{-m}(\theta_x, \phi_x)\bar{Y}_{l'}^{m'}(\theta_x, \phi_x) \\
&= \frac{(4\pi)^2}{(2l+1)(2l'+1)}\sum_{m=-l}^l\sum_{m'=-l'}^{l'}(-1)^m Y_l^m(\theta_k, \phi_k)Y_{l'}^{m'}(\theta_k, \phi_k)\delta_{ll'}\delta_{-mm'},
\end{aligned} \tag{A.32}$$

then we have

$$\begin{aligned}
\int d\Omega_x e^{-i\mathbf{k}\cdot\mathbf{x}} &= \sum_{l=0}^{\infty}\sum_{l'=0}^{\infty}(-i)^{l+l'}(2l+1)(2l'+1)j_l\left(\frac{1}{2}kr(c+a)\right) \\
&\quad \times j_{l'}\left(\frac{1}{2}kr(c-a)\right)\int d\Omega_x P_l(\cos\gamma)P_{l'}(\cos\gamma) \\
&= 16\pi^2\sum_{l=0}^{\infty}\sum_{m=-l}^l(-1)^{l+m}j_l\left(\frac{1}{2}kr(c+a)\right)j_l\left(\frac{1}{2}kr(c-a)\right) \\
&\quad \times Y_l^m(\theta_k, \phi_k)Y_l^{-m}(\theta_k, \phi_k).
\end{aligned} \tag{A.33}$$

Therefore,

$$\begin{aligned}
\tilde{\delta}(\mathbf{k}) &= a^2 c \bar{\delta} \int_0^1 r^2 dr \int d\Omega e^{-i\mathbf{k} \cdot \mathbf{x}} \\
&= 16\pi^2 a^2 c \bar{\delta} \sum_{l=0}^{\infty} \sum_{m=-l}^l (-1)^{l+m} Y_l^m(\theta_k, \phi_k) Y_l^{-m}(\theta_k, \phi_k) \\
&\quad \times \int_0^1 r^2 dr j_l\left(\frac{1}{2}kr(c+a)\right) j_l\left(\frac{1}{2}kr(c-a)\right),
\end{aligned} \tag{A.34}$$

and integrating over $r \in [0, 1]$, we have

$$\begin{aligned}
\tilde{\delta}(\mathbf{k}) &= -\frac{8\pi^3 a \bar{\delta}}{\sqrt{c^2 - a^2} k^2} \sum_{l=0}^{\infty} \sum_{m=-l}^l (-1)^{l+m} Y_l^m(\theta_k, \phi_k) Y_l^{-m}(\theta_k, \phi_k) \\
&\quad \times \left[(c+a) J_{l-\frac{1}{2}}\left(\frac{1}{2}k(c+a)\right) J_{l+\frac{1}{2}}\left(\frac{1}{2}k(c-a)\right) \right. \\
&\quad \left. - (c-a) J_{l-\frac{1}{2}}\left(\frac{1}{2}k(c-a)\right) J_{l+\frac{1}{2}}\left(\frac{1}{2}k(c+a)\right) \right].
\end{aligned} \tag{A.35}$$

We Taylor expand the above equation for $\tilde{\delta}(\mathbf{k})$ about $\epsilon \simeq 0$ up to a linear order.

$$\begin{aligned}
\tilde{\delta}(\mathbf{k}) &\simeq \frac{a\pi^3 \bar{\delta}}{k^2} \sum_{l=0}^{\infty} \frac{(ka)^{l+1/2}}{2^{2l-3/2} \Gamma(l+3/2)} \epsilon^l \left[ka \epsilon J_{l+\frac{1}{2}}(ka) + \{2 + (l-1)\epsilon\} J_{l+\frac{3}{2}}(ka) \right] \\
&\quad \times \sum_{m=-l}^l (-1)^{l+m} Y_l^m(\theta_k, \phi_k) Y_l^{-m}(\theta_k, \phi_k)
\end{aligned} \tag{A.36}$$

For a prolate ellipsoid, where $a < c$ and $\epsilon \equiv 1 - \frac{a}{c}$,

$$\tilde{\delta}(\mathbf{k}) \simeq 4\pi \bar{\delta} a^3 \left[\frac{j_1(ka)}{ka} + \epsilon \left(\frac{j_1(ka)}{ka} - j_2(ka) \right) \right] + \mathcal{O}(\epsilon^2). \tag{A.37}$$

For an oblate ellipsoid, where $a > c$ and $\epsilon \equiv 1 - \frac{c}{a}$,

$$\tilde{\delta}(\mathbf{k}) \simeq 4\pi \bar{\delta} a^3 \left[\frac{j_1(ka)}{ka} - \epsilon \left(\frac{j_1(ka)}{ka} - j_2(ka) \right) \right] + \mathcal{O}(\epsilon^2). \tag{A.38}$$

Therefore, eq. (A.12) becomes

$$\begin{aligned}
\kappa(\mathbf{x}) &= \frac{4\pi a^3 f \bar{\delta}}{x_3} \int_0^{\infty} \frac{dk}{(2\pi)^3} i k \left[\frac{j_1(ka)}{ka} \pm \epsilon \left(\frac{j_1(ka)}{ka} - j_2(ka) \right) \right] \\
&\quad \int d\Omega_k \cos \theta_k e^{i\mathbf{k} \cdot \mathbf{x}},
\end{aligned} \tag{A.39}$$

where

$$\begin{aligned}
\int d\Omega_k \cos \theta_k e^{i\mathbf{k} \cdot \mathbf{x}} &= \sum_{l=0}^{\infty} \sum_{l'=0}^{\infty} \sqrt{\frac{4\pi}{3}} (-i)^{l+l'} (2l+1)(2l'+1) j_l\left(-\frac{1}{2}kr(c+a)\right) \\
&\quad \times j_{l'}\left(-\frac{1}{2}kr(c-a)\right) \int d\Omega_k Y_1^0(\theta_k, \phi_k) P_l(\cos \gamma) P_{l'}(\cos \gamma).
\end{aligned} \tag{A.40}$$

Using the addition theorem given in eq. (A.17), we rewrite the above equation,

$$\begin{aligned}
\int d\Omega_k \cos \theta_k e^{i\mathbf{k}\cdot\mathbf{x}} &= \sum_{l=0}^{\infty} \sum_{l'=0}^{\infty} \sum_{m=-l}^l \sum_{m'=-l'}^{l'} (4\pi)^2 \sqrt{\frac{4\pi}{3}} (-i)^{l+l'} j_l \left(-\frac{1}{2}kr(c+a) \right) \\
&\times j_{l'} \left(-\frac{1}{2}kr(c-a) \right) (-1)^{m+m'} Y_l^{-m}(\theta_x, \phi_x) Y_{l'}^{-m'}(\theta_x, \phi_x) \\
&\times \int d\Omega_k Y_1^0(\theta_k, \phi_k) Y_l^m(\theta_k, \phi_k) Y_{l'}^{m'}(\theta_k, \phi_k).
\end{aligned} \tag{A.41}$$

Here,

$$\begin{aligned}
&j_l \left(-\frac{1}{2}kr(c+a) \right) j_{l'} \left(-\frac{1}{2}kr(c-a) \right) \\
&\simeq 2^{-2l'-\frac{5}{2}} \pi \frac{(-1)^{l+l'}}{\Gamma(l'+\frac{3}{2})} (kra)^{l'-\frac{1}{2}} \epsilon^{l'} \\
&\times \left[\{2 + (l+2l')\epsilon\} J_{l+\frac{1}{2}}(kra) - kra\epsilon J_{l+\frac{3}{2}}(kra) \right] \\
&= 2^{-2(l'+1)} \frac{\sqrt{\pi}(-1)^{l+l'}}{\Gamma(l'+\frac{3}{2})} (kra)^{l'} \epsilon^{l'} \left[\{2 + (l+2l')\epsilon\} j_l(kra) - kra\epsilon j_{l+1}(kra) \right]
\end{aligned} \tag{A.42}$$

for a prolate ellipsoid ($c > a$), and

$$\begin{aligned}
&j_l \left(-\frac{1}{2}kr(c+a) \right) j_{l'} \left(-\frac{1}{2}kr(c-a) \right) \\
&\simeq 2^{-2l'-\frac{5}{2}} \pi \frac{(-1)^l}{\Gamma(l'+\frac{3}{2})} (kra)^{l'-\frac{1}{2}} \epsilon^{l'} \left[(2-l\epsilon) J_{l+\frac{1}{2}}(kra) + kra\epsilon J_{l+\frac{3}{2}}(kra) \right] \\
&= 2^{-2(l'+1)} \frac{\sqrt{\pi}(-1)^l}{\Gamma(l'+\frac{3}{2})} (kra)^{l'} \epsilon^{l'} \left[(2-l\epsilon) j_l(kra) + kra\epsilon j_{l+1}(kra) \right]
\end{aligned} \tag{A.43}$$

for an oblate ellipsoid ($c < a$). In order to truncate the equation at linear order in ϵ , we have $l' \leq 1$, such that

$$\begin{aligned}
&j_l \left(-\frac{1}{2}kr(c+a) \right) j_{l'} \left(-\frac{1}{2}kr(c-a) \right) \\
&\simeq \begin{cases} \frac{1}{2}(-1)^l [(2+l\epsilon)j_l(kra) - kra\epsilon j_{l+1}(kra)] & \text{for } l' = 0 \\ -\frac{1}{6}(-1)^l kra\epsilon j_l(kra) & \text{for } l' = 1 \\ \mathcal{O}(\epsilon^2) & \text{otherwise} \end{cases}
\end{aligned} \tag{A.44}$$

for a prolate ellipsoid, and

$$\begin{aligned}
&j_l \left(-\frac{1}{2}kr(c+a) \right) j_{l'} \left(-\frac{1}{2}kr(c-a) \right) \\
&\simeq \begin{cases} \frac{1}{2}(-1)^l [(2-l\epsilon)j_l(kra) + kra\epsilon j_{l+1}(kra)] & \text{for } l' = 0 \\ \frac{1}{6}(-1)^l kra\epsilon j_l(kra) & \text{for } l' = 1 \\ \mathcal{O}(\epsilon^2) & \text{otherwise} \end{cases}
\end{aligned} \tag{A.45}$$

for an oblate ellipsoid.

As for the integration over the solid angle, Ω_k , we have

$$\begin{aligned} & \int d\Omega_k Y_1^0(\theta_k, \phi_k) Y_l^m(\theta_k, \phi_k) Y_{l'}^{m'}(\theta_k, \phi_k) \\ &= \sqrt{\frac{3(2l+1)(2l'+1)}{4\pi}} \begin{pmatrix} 1 & l & l' \\ 0 & 0 & 0 \end{pmatrix} \begin{pmatrix} 1 & l & l' \\ 0 & m & m' \end{pmatrix}, \end{aligned} \quad (\text{A.46})$$

where the Wigner-3J symbol must satisfy the triangular inequality such that $|1-l| \leq l' \leq 1+l$, and $0+m = -m'$ in order to have a non-zero value.

As for eq. (A.41), since $l' \leq 1$, we have a limited number of non-zero terms. We have $(l, l', m, m') = (0, 1, 0, 0)$, $(1, 0, 0, 0)$, $(2, 1, -1, 1)$, $(2, 1, 0, 0)$ and $(2, 1, 1, -1)$ as the non-zero terms. We rewrite eq. (A.41) with a finite number of terms truncating $\mathcal{O}(\epsilon^2)$ and higher as follows,

$$\begin{aligned} \int d\Omega_k \cos \theta_k e^{i\mathbf{k} \cdot \mathbf{x}} &\simeq \frac{(4\pi)^2}{\sqrt{3}} i \left[\pm \frac{1}{6} kra \epsilon j_0(kra) Y_0^0(\theta_x, \phi_x) Y_1^0(\theta_x, \phi_x) \right. \\ &+ \frac{1}{2} \{ (2 \pm \epsilon) j_1(kra) \mp kra \epsilon j_2(kra) \} Y_0^0(\theta_x, \phi_x) Y_1^0(\theta_x, \phi_x) \\ &\pm \frac{1}{6} kra \epsilon j_2(kra) \left\{ \sqrt{\frac{3}{5}} Y_1^{-1}(\theta_x, \phi_x) Y_2^1(\theta_x, \phi_x) \right. \\ &\left. \left. + \sqrt{\frac{3}{5}} Y_1^1(\theta_x, \phi_x) Y_2^{-1}(\theta_x, \phi_x) - \frac{2}{\sqrt{5}} Y_1^0(\theta_x, \phi_x) Y_2^0(\theta_x, \phi_x) \right\} \right] \end{aligned} \quad (\text{A.47})$$

Here, in the limit of $\epsilon \rightarrow 0$, we recover

$$\int d\Omega_k \cos \theta_k e^{i\mathbf{k} \cdot \mathbf{x}} = \frac{(4\pi)^2}{\sqrt{3}} i j_1(kra) Y_0^0(\theta_x, \phi_x) Y_1^0(\theta_x, \phi_x) = 4\pi i j_1(kra) \cos \theta_x, \quad (\text{A.48})$$

as in eq. (A.19).

Finally, from eq. (A.39) and (A.47), and truncating $\mathcal{O}(\epsilon^2)$ and higher terms, we have

$$\begin{aligned}
\kappa(\mathbf{x}) &= \frac{4\pi a^3 f \bar{\delta}}{x_3} \int_0^\infty \frac{dk}{(2\pi)^3} ik \left[\frac{j_1(ka)}{ka} + \epsilon \left(\frac{j_1(ka)}{ka} - j_2(ka) \right) \right] \\
&\times \int d\Omega_k \cos \theta_k e^{i\mathbf{k} \cdot \mathbf{x}} \\
&\simeq -\frac{8f\bar{\delta}a^3}{\sqrt{3}x_3} \left[\frac{r}{6} \epsilon Y_0^0(\theta_x, \phi_x) Y_1^0(\theta_x, \phi_x) \int_0^\infty dk k j_1(ka) j_0(kra) \right. \\
&+ \frac{2+\epsilon}{2a} Y_0^0(\theta_x, \phi_x) Y_1^0(\theta_x, \phi_x) \int_0^\infty dk j_1(ka) j_1(kra) \\
&- \frac{r}{2} \epsilon Y_0^0(\theta_x, \phi_x) Y_1^0(\theta_x, \phi_x) \int_0^\infty dk k j_1(ka) j_2(kra) \\
&+ \frac{r}{6} \epsilon \left\{ \sqrt{\frac{3}{5}} Y_1^{-1}(\theta_x, \phi_x) Y_2^1(\theta_x, \phi_x) + \sqrt{\frac{3}{5}} Y_1^1(\theta_x, \phi_x) Y_2^{-1}(\theta_x, \phi_x) \right. \\
&- \left. \frac{2}{\sqrt{5}} Y_1^0(\theta_x, \phi_x) Y_2^0(\theta_x, \phi_x) \right\} \int_0^\infty dk k j_1(ka) j_2(kra) \\
&+ \frac{\epsilon}{a} Y_0^0(\theta_x, \phi_x) Y_1^0(\theta_x, \phi_x) \int_0^\infty dk j_1(ka) j_1(kra) \\
&- \left. \epsilon Y_0^0(\theta_x, \phi_x) Y_1^0(\theta_x, \phi_x) \int_0^\infty dk k j_2(ka) j_1(kra) \right].
\end{aligned} \tag{A.49}$$

Taking integrations over k (see appendix §B),

$$\begin{aligned}
\kappa(\mathbf{x}) &\simeq -\frac{f\bar{\delta}}{3} \frac{ar \cos \theta_x}{x_3} (1 - \epsilon) \\
&= -\frac{f\bar{\delta}}{3} \frac{a}{c} (1 - \epsilon) \\
&= -\frac{f\bar{\delta}}{3} (1 - \epsilon)^2 \\
&\simeq -\frac{f\bar{\delta}}{3} (1 - 2\epsilon)
\end{aligned} \tag{A.50}$$

Similarly, for an oblate spheroid,

$$\kappa(\mathbf{x}) \simeq -\frac{f\bar{\delta}}{3} (1 + 2\epsilon) \tag{A.51}$$

As we compare against numerical calculations of $\kappa(\mathbf{x})$, we see $\kappa(\mathbf{x}) \simeq -\frac{f\bar{\delta}}{3} (1 \mp \epsilon)$ fits the result better for both prolate and oblate spheroids.

We see how real space geometry of a given void affects the peculiar velocity field within the void by comparing Eqs.(A.20) and (A.50). As for a prolate spherical void, we set the longest principal axis, $a < c \equiv a/(1 - \epsilon)$, to lie along the line of sight. As discussed by Icke [14], originally aspherical voids tend to become a sphere with a slower expansion speed along the longest principal axis, and vice versa. For a given prolate spheroidal void with its longest principal axis along the line of sight, peculiar velocity along the largest axis become smaller as we increase ellipticity. Since the deformation of the void shape in the redshift space, $\kappa(\mathbf{x})$,

is proportional to the peculiar velocity, an aspherical void in real space with the longest axis being along the line of sight experiences less deformation compared to an originally spherical void.

Also, we see that the degree of deformation of an aspherical void in the redshift space, $\kappa(\mathbf{x})$, is independent of the size of the void, but dependent only on the linear growth factor, $f \equiv \frac{d \ln D}{d \ln a}$, the mean density contrast of the void, $\bar{\delta}$, and the ellipticity of the void in the real space.

B List of Y_l^m , j_l and Wigner-3J symbols used in appendix A

Here, we collect the properties of the spherical harmonics, $Y_l^m(\theta, \phi)$, spherical Bessel functions, $j_l(z)$, Gamma functions, $\Gamma(x)$, and the Wigner-3J symbols, $\begin{pmatrix} j_1 & j_2 & j_3 \\ m_1 & m_2 & m_3 \end{pmatrix}$, that are used in our calculations.

$$Y_0^0(\theta, \phi) = \frac{1}{2\sqrt{\pi}} \quad (\text{B.1})$$

$$Y_1^{-1}(\theta, \phi) = \frac{1}{2} \sqrt{\frac{3}{2\pi}} \sin \theta e^{-i\phi} \quad (\text{B.2})$$

$$Y_1^0(\theta, \phi) = \frac{1}{2} \sqrt{\frac{3}{\pi}} \cos \theta \quad (\text{B.3})$$

$$Y_1^1(\theta, \phi) = -\frac{1}{2} \sqrt{\frac{3}{2\pi}} \sin \theta e^{i\phi} \quad (\text{B.4})$$

$$j_0(z) = \frac{\sin z}{z} \quad (\text{B.5})$$

$$j_1(z) = \frac{\sin z}{z^2} - \frac{\cos z}{z} \quad (\text{B.6})$$

$$j_2(z) = \left(\frac{3}{z^3} - \frac{1}{z} \right) \sin z - \frac{3}{z^2} \cos z \quad (\text{B.7})$$

$$j_3(z) = \left(\frac{15}{z^4} - \frac{6}{z^2} \right) \sin z - \left(\frac{15}{z^3} - \frac{1}{z} \right) \cos z \quad (\text{B.8})$$

$$\Gamma(1/2) = \sqrt{\pi} \quad (\text{B.9})$$

$$\Gamma(3/2) = \frac{\sqrt{\pi}}{2} \quad (\text{B.10})$$

$$\Gamma(5/2) = \frac{3\sqrt{\pi}}{4} \quad (\text{B.11})$$

$$\Gamma(7/2) = \frac{15\sqrt{\pi}}{8} \quad (\text{B.12})$$

$$\Gamma(9/2) = \frac{105\sqrt{\pi}}{16} \quad (\text{B.13})$$

$$\begin{pmatrix} 1 & 0 & 1 \\ 0 & 0 & 0 \end{pmatrix} = -\frac{1}{\sqrt{3}} \quad (\text{B.14})$$

$$\begin{pmatrix} 1 & 1 & 0 \\ 0 & 0 & 0 \end{pmatrix} = -\frac{1}{\sqrt{3}} \quad (\text{B.15})$$

$$\begin{pmatrix} 1 & 2 & 1 \\ 0 & 0 & 0 \end{pmatrix} = \sqrt{\frac{2}{15}} \quad (\text{B.16})$$

$$\begin{pmatrix} 1 & 2 & 1 \\ 0 & -1 & 1 \end{pmatrix} = -\frac{1}{\sqrt{10}} \quad (\text{B.17})$$

$$\begin{pmatrix} 1 & 2 & 1 \\ 0 & 1 & -1 \end{pmatrix} = -\frac{1}{\sqrt{10}} \quad (\text{B.18})$$

For $0 < r < 1$ and $a > 0$,

$$\int_0^\infty dk \, j_1(ka) j_1(kra) = \frac{\pi r}{6a} \quad (\text{B.19})$$

$$\int_0^\infty dk \, k \, j_2(ka) j_1(kra) = \frac{\pi r}{2a^2} \quad (\text{B.20})$$

$$\int_0^\infty dk \, k \, j_1(ka) j_0(kra) = \frac{\pi}{2a^2} \quad (\text{B.21})$$

$$\int_0^\infty dk \, k \, j_1(ka) j_2(kra) = 0 \quad (\text{B.22})$$

References

- [1] Acquaviva, V. & Gawiser, E. 2010, Physical Review D, 82, 082001
- [2] Alcock, C. & Paczynski, B. 1979, Nature, 281, 358
- [3] Colberg, J. M., Sheth, R. K., Diaferio, A., Gao, L., & Yoshida, N. 2005, Mon. Not. R. Astron. Soc., 360, 216
- [4] Colberg, J. M., et al. 2008, Mon. Not. R. Astron. Soc., 387, 933
- [5] Croton, D. J., et al. 2006, Mon. Not. R. Astron. Soc., 365, 11
- [6] De Lucia, G. & Blaizot, J. 2007, Mon. Not. R. Astron. Soc., 375, 2
- [7] Doroshkevich, A. G. 1970, Astrophysics, 6, 320
- [8] Foster, C. & Nelson, L. A. 2009, Astrophys. Journal, 699, 1252
- [9] Franx, M., Illingworth, G., & de Zeeuw, T. 1991, Astrophys. Journal, 383, 112
- [10] Guzzo, L., et al. 2008, Nature, 451, 541
- [11] Hamilton, A. J. S. 2001, Mon. Not. R. Astron. Soc., 322, 419
- [12] Hoyle, F. & Vogeley, M. S. 2002, Astrophys. Journal, 566, 641
- [13] Hui, L. & Bertschinger, E. 1996, Astrophys. Journal, 471, 1
- [14] Icke, V. 1984, Mon. Not. R. Astron. Soc., 206, 1P
- [15] Jang-Condell, H. & Hernquist, L. 2001, Astrophys. Journal, 548, 68
- [16] Kaiser, N. 1987, Mon. Not. R. Astron. Soc., 227, 1

- [17] Kazin, E. A., Sánchez, A. G., & Blanton, M. R. 2012, *Mon. Not. R. Astron. Soc.*, 419, 3223
- [18] Komatsu, E., et al. 2009, *Astrophys. JournalSuppl.*, 180, 330
- [19] Lavaux, G. & Wandelt, B. D. 2010, *Mon. Not. R. Astron. Soc.*, 403, 1392
- [20] —. 2011, ArXiv e-prints
- [21] Lee, J. & Park, D. 2009, *Astrophys. J. Lett.*, 696, L10
- [22] Lewis, A., Challinor, A., & Lasenby, A. 2000, *Astrophys. Journal*, 538, 473
- [23] Lightman, A. P. & Schechter, P. L. 1990, *Astrophys. J. Suppl.*, 74, 831
- [24] Linder, E. V. & Jenkins, A. 2003, *Mon. Not. R. Astron. Soc.*, 346, 573
- [25] Maeda, K.-i., Sakai, N., & Triay, R. 2011, *Journal of Cosmology and Astroparticle Physics*, 8, 26
- [26] Pan, D. C., Vogeley, M. S., Hoyle, F., Choi, Y.-Y., & Park, C. 2011, ArXiv e-prints
- [27] Park, D. & Lee, J. 2007, *Physical Review Letters*, 98, 081301
- [28] Patiri, S. G., Prada, F., Holtzman, J., Klypin, A., & Betancort-Rijo, J. 2006, *Mon. Not. R. Astron. Soc.*, 372, 1710
- [29] Peebles, P. J. E. 1980, *The large-scale structure of the universe* (Research supported by the National Science Foundation. Princeton, N.J., Princeton University Press, 1980. 435 p.)
- [30] Perlmutter, S., et al. 1999, *Astrophys. Journal*, 517, 565
- [31] Platen, E., van de Weygaert, R., & Jones, B. J. T. 2008, *Mon. Not. R. Astron. Soc.*, 387, 128
- [32] Riess, A. G., et al. 1998, *Astron. J.*, 116, 1009
- [33] Ryden, B. S. 1995, *Astrophys. Journal*, 452, 25
- [34] Ryden, B. S. & Melott, A. L. 1996, *Astrophys. Journal*, 470, 160
- [35] Schmidt, J. D., Ryden, B. S., & Melott, A. L. 2001, *Astrophys. Journal*, 546, 609
- [36] Sheth, R. K. & van de Weygaert, R. 2004, *Mon. Not. R. Astron. Soc.*, 350, 517
- [37] Shoji, M., Jeong, D., & Komatsu, E. 2009, *Astrophys. Journal*, 693, 1404
- [38] Simpson, F. & Peacock, J. A. 2010, *Physical Review D*, 81, 043512
- [39] Springel, V., et al. 2005, *Nature*, 435, 629
- [40] Wang, L. & Steinhardt, P. J. 1998, *Astrophys. Journal*, 508, 483
- [41] White, S. D. M. 1979, *Mon. Not. R. Astron. Soc.*, 186, 145